

**LOW-NOISE STRETCHABLE ORGANIC PHOTODIODE USING
AN ELASTOMERIC BULK HETEROJUNCTION**

A Dissertation
Presented to
The Academic Faculty

by

Youngrak Park

In Partial Fulfillment
of the Requirements for the Degree
Doctor of Philosophy in the
School of Electrical and Computer Engineering

Georgia Institute of Technology
DECEMBER 2021

COPYRIGHT © 2021 BY YOUNGRAK PARK

LOW-NOISE STRETCHABLE ORGANIC PHOTODIODE USING AN ELASTOMERIC BULK HETEROJUNCTION

Approved by:

Dr. Bernard Kippelen, Advisor
School of Electrical and Computer
Engineering
Georgia Institute of Technology

Dr. Shyh-Chiang Shen
School of Electrical and Computer
Engineering
Georgia Institute of Technology

Dr. Omer Inan
School of Electrical and Computer
Engineering
Georgia Institute of Technology

Dr. Olivier Pierron
School of Mechanical Engineering
Georgia Institute of Technology

Dr. Oliver Brand
School of Electrical and Computer
Engineering
Georgia Institute of Technology

Date Approved: [Dec 10th, 2021]

ACKNOWLEDGEMENTS

I would like to express my sincere gratitude to my advisor, Professor Bernard Kippelen, for his continuous support and guidance. He has played an important role in my research and work. His guidance inspired me in many ways, not only in academic research, but also in life. I am sure what I learned from him during Ph.D. will be of great help to me for the rest of my life. Also, I would like to thank my committee members, Dr. Inan, Dr. Brand, Dr. Shen, and Dr. Pierron for their valuable time and advice and serving on my committee.

I would like to thank Dr. Canek Fuentes-Hernandez for his willingness to help, feedback, and immeasurable source of knowledge. Without his insights, my research would have been entirely different. I have also benefited greatly from the numerous discussions with past and present group member: Dr Xiaojia Jia, Dr. Wen-Fang Chou, Dr. Xiaoqing Zhang, Dr. Felipe Larrain, Dr. Victor Rodriguez-Toro, Dr. Silja Abraham, Yi-Chien Chang, Gunhee Kim, Oliver Moreno, and Jingwei Yang. I am very indebted to my collaborators: Dr. Junxiang Zhang, Mingu Kim, Kyungjin Kim, Dr. Seth Marder, and Dr Samuel Graham.

This work was funded by National Nuclear Security Administration (NNSA), and Consortium for Nonproliferation Enabling Capabilities (CNEC).

I would like to finish by expressing how thankful I am for the spiritual support of my family and friends in Korea. I owe my Ph.D. completion to their supports and numerous sacrifices. This dissertation is dedicated to all of them.

TABLE OF CONTENTS

ACKNOWLEDGEMENTS	iii
LIST OF TABLES	vii
LIST OF FIGURES	viii
LIST OF SYMBOLS AND ABBREVIATIONS	x
SUMMARY	xiv
CHAPTER 1. Introduction	1
1.1 Wearable and Biomedical Optoelectronics	1
1.2 Early Development in Flexible Optoelectronics	2
1.3 Imparting Stretchability to Organic Semiconductors	3
1.4 Development of Organic Photodiodes (OPD)	5
1.5 Recent Advances in Stretchable OPDs	6
1.6 Structure of the Dissertation	8
CHAPTER 2. Organic Semiconductors and Stretchable Organic Photodiodes	9
2.1 Semiconductor Device Physics	9
2.2 Organic Semiconductors	15
2.3 Working Principles of OPDs	20
2.3.1 Photoactive Layer	20
2.3.2 Device Structure	22
2.4 Performance Metrics of Stretchable OPDs	26
2.4.1 Responsivity	26
2.4.2 Noise	26
2.4.3 Noise Equivalent Power and Specific detectivity	27
2.4.4 Response Time	29
2.4.5 Mechanical Properties of Films	30
CHAPTER 3. Experimental Methods and Modeling	33
3.1 Materials	33
3.2 Fabrication	36
3.2.1 Fabrication of Freestanding Films	36
3.2.2 Fabrication of Rigid Photodiodes with elastomeric BHJ (e-BHJ)	37
3.2.3 Fabrication of elastomeric OPD (e-OPD)	39
3.3 Characterization	41
3.3.1 Photodetector Characterization	41
3.3.2 Mechanical Characterization	44
3.4 Equivalent Circuit Model	46
CHAPTER 4. Rigid Photodiodes with Elastomeric Bulkheterojunction	48
4.1 Introduction	48
4.2 Optoelectrical Characteristics of Rigid Photodiodes with e-BHJ	49

4.2.1	Optimization of SEBS Contents	49
4.2.2	Equivalent Circuit Analysis	51
4.2.3	Photodetector Characteristics	55
4.2.4	Response Time	59
CHAPTER 5.	Fully stretchable Organic Photodiodes (e-OPD)	62
5.1	Introduction	62
5.2	Mechanical characteristics of e-BHJ Film	63
5.3	Stretchable Electrodes	67
5.4	Optoelectrical characteristics of e-OPDs	73
5.4.1	Photodetector characteristics	73
5.4.2	Response Time	79
5.5	Operational Stability in Ambient Air	82
CHAPTER 6.	Conclusion and Future Work	84
6.1	Conclusion	84
6.2	Future Work	86
6.2.1	Monitoring Photoplethysmogram (PPG)	86
6.2.2	Phosphomolybdic Acid (PMA) Doping	86
6.2.3	Stretchable OPV Device	87
REFERENCES		88

LIST OF TABLES

Table 1 Physical parameters of OPDs derived from the equivalent circuit model.	54
Table 2 Mechanical properties of freestanding films extracted from the stress-strain plots.	67

LIST OF FIGURES

Figure 1 Young's modulus scales	3
Figure 2 Orbital structures of (a) Carbon atom, (b) Ethylene molecule.	15
Figure 3 Energy diagram of (a) Ethylene, (b) Butadiene.....	17
Figure 4 Energy level diagram in organic solid bulk.....	19
Figure 5 Schematic diagram of BHJ formation.	20
Figure 6 Schematic and energy diagram of the formation of charge-transfer states.	22
Figure 7 Device structure of OPD.	23
Figure 8 Energy level diagrams of OPDs under (a) Dark (b) Illumination.	24
Figure 9 Derivation of electronic noise current from rms current.	28
Figure 10 The response time measurement.	30
Figure 11 Tensile test diagram and curve.	31
Figure 12 Chemical structure of materials.....	35
Figure 13 The device structure of elastomeric OPD.....	38
Figure 14 Schematics of the fabrication process of e-OPD.....	40
Figure 15 Schematic of extracting rms electronic noise current measurement	41
Figure 16 Schematic of response time measurement.....	43
Figure 17 (a) Equivalent circuit model of a photodiode. (b) J-V characteristics of Equivalent circuit model	47
Figure 18 <i>I</i> - <i>V</i> characteristics of OPDs with SEBS contents of 33 wt.%, 50 wt.%, and 67 wt.%, respectively, (a) measured with an optical power of 100 nW at 653 nm, (b) measured under dark.	50
Figure 19 Spectral absorption (1-transmittance) of BHJs on glass.....	51
Figure 20 Comparison of the dark current density of OPDs measured in the dark. The shaded area represents the range from maximum to minimum dark current density values for samples of the same structure.....	52
Figure 21 Analysis of dark current density of OPDs. (a) Equivalent circuit model of OPD. (b) Comparison of measured and simulated dark current density of champion OPDs.....	53
Figure 22 Dark current density (top) and root-mean-squared noise box plot (<i>N</i> = # of data points) (bottom). The device structure of OPD (inset)	55
Figure 23 Analysis of photodetector metrics for OPD with e-BHJ on a rigid substrate. (a) Optical power dependence of transient current and photocurrent. (b) Optical power dependence of signal-to-noise ratio.	56

Figure 24 Photocurrent (top) and responsivity (bottom) vs. optical power at a wavelength of 653 nm.	58
Figure 25 Measured responsivity spectra of OPD with e-BHJ (top). Specific detectivity spectra for the elastomeric OPD normalized at a wavelength of 653 nm using responsivity spectra (bottom).....	59
Figure 26 Response time of OPD with e-BHJ.	60
Figure 27 Frequency response of OPD with e-BHJ.....	61
Figure 28 (a) Chemical structure of materials used in r-BHJ and e-BHJ film. (b) A photograph of the relaxed and strained (189 %) e-BHJ film in water.	63
Figure 29 (a) Stress (σ) vs. strain (ϵ) behavior of r-BHJ, e-BHJ, and SEBS from the uniaxial tensile test. (b) Range of Young's moduli (E) using different stress-strain definitions. The error bars represent the minimum and maximum bounds of E (top). Strain at break compared to the initial length (bottom).	65
Figure 30 (a) Comparison of experimental and fitted stress curve of e-BHJ. (b) Elasticity vs. strain plot derived from the engineering stress-strain curve.	66
Figure 31 (a) Structure of pre-strained PDMS/PEDOT:PSS electrode. (b) Normalized resistance vs. strain plot.	69
Figure 32 Optical microscopy image for 30% pre-strained PDMS/PEDOT:PSS under different strains	70
Figure 33 Optical microscopy image for 60% pre-strained PDMS/PEDOT:PSS under different strains	72
Figure 34 Dark current (top) and root-mean-squared noise box plot (bottom) under different strains.	73
Figure 35 Optical power-dependent photocurrent (top) and responsivity (bottom) under different strains	75
Figure 36 Analysis of photodetector metrics for unstrained e-OPD. (a) Optical power dependence of transient current and photocurrent. (b) Optical power dependence of signal-to-noise ratio.	76
Figure 37 Noise equivalent power (top) and specific detectivity (bottom) under different strains	77
Figure 38 Dark current (top) and root-mean-squared noise box plot (bottom) of e-OPD using 60% pre-strained PDMS/PEDOT:PSS.....	79
Figure 39 Response time of e-OPD under different strains. (a) 10%-90% response time. (b) Frequency-dependent normalized responsivity.....	80
Figure 40 (a) Structure of e-OPD with encapsulation (b) Normalized responsivity vs. Exposure time under different conditions.....	82

LIST OF SYMBOLS AND ABBREVIATIONS

HOMO	Highest Occupied Molecular Orbital
LOMO	Lowest Unoccupied Molecular Orbital
E_g	Energy gap
E_{trans}	Transport gap
E_{opt}	Optical gap
E_B	Binding energy
IP	Ionization potential
EA	Electron affinity
OPD	Organic photodiode
BHJ	Bulk heterojunction
CT	Charge-transfer state
OPV	Organic photovoltaics
OFET	Organic field-effect transistor
V_{oc}	Open-circuit voltage
I_{sc}	Short-circuit current
EQE	External Quantum Efficiency
FF	Fill Factor
PCE	Power Conversion Efficiency
PPG	Photoplethysmogram
E	Young's modulus
SEBS	Polystyrene-block-poly(ethylene-ranbutylene)-block-polystyrene
PTB7	Poly(thieno[3,4-b]-thiophene/benzodithiophene)
DIO	Diiodooctane
PEIE	Polyethylenimine, 80% ethoxylated
ITO	Indium tin oxide
e-BHJ	Elastomeric bulk heterojunction
r-BHJ	Reference bulkheterojunction

AFM	Atomic Force Microscopy
I_{rms}	Root-mean-squared electronic noise current
NEP	Noise equivalent power
D^*	Specific detectivity
J_0	Saturation current density
n	Diode ideality factor
R_pA	Shunt resistance
R_sA	Series resistance
D^*	Specific detectivity
PEDOT:PSS	Poly(3,4-ethylenedioxythiophene):Polystyrene sulfonate
PTDB-TF	Poly[(2,6-(4,8-bis(5-(2-ethylhexyl-3-fluoro)thiophen-2-yl)-benzo[1,2-b:4,5-b']dithiophene))-alt-(5,5-(1',3'-di-2-thienyl-5',7'-bis(2-ethylhexyl)benzo[1',2'-c:4',5'-c']dithiophene-4,8-dione)]
Y6	2,20 -((2Z,20 Z)-((12,13-bis(2-ethylhexyl)-3,9-diundecyl-12,13-dihydro-[1,2,5]thiadiazolo[3,4-e]thieno[2,"30 ':4',50] thieno[20 ,30 :4,5]pyrrolo[3,2-g]thieno[20 ,30 :4,5]thieno[3,2-b]indole-2,10-diyl)bis(methanylylidene))bis(5,6-difluoro-3-oxo-2,3-dihydro-1H-indene-2,1-diylidene))dimalononitrile
MEH-PPV	poly(phenylene-vinylene)
P3OT	poly(3-octyl thiophene)
T	Absolute temperature
\mathfrak{R}	Responsivity
E_F	Fermi level energy
k	Boltzmann constant
n_0	Intrinsic electron concentration
p_0	Intrinsic hole concentration
E_C	Energy at the conduction band edge
E_V	Energy at the valence band edge
F_n	Quasi-Fermi level energy for electrons
F_p	Quasi-Fermi level energy for electrons
E_i	Intrinsic Fermi level energy
q	Elementary charge

μ_n	Mobility of electrons
μ_p	Mobility of holes
D_n	Electron diffusion coefficient
D_p	Hole diffusion coefficient
V_{ph}	Photovoltage
I_{ph}	Photocurrent
P_{in}	Incident optical power
λ	Wavelength
h	Planck constant
c	Speed of light
S_{shot}	Shot noise
$S_{thermal}$	Thermal noise
$S_{1/f}$	$1/f$ noise
S_n	Noise power spectral density
τ_{drift}	Field-dependent carrier transit time
τ_{diff}	Diffusion time before recombination
τ_{RC}	RC time delay associated with effects of the external circuit
σ	Stress
F	Applied force
ε	Strain
PEDOT:PSS	Poly(3,4-ethylenedioxythiophene):polystyrene sulfonate
EGaIn	Eutectic Gallium-Indium
P3HT	Poly(3-hexylthiophene-2,5-diyl)
ICBA	Indene C60-bisadduct
PCBM	[6,6]-Phenyl C61 butyric acid methyl ester
PEIE	Polyethylenimine-ethoxylated
PDMS	Polydimethylsiloxane
e-OPD	elastomeric organic photodiode
SNR	Signal-to-noise ratio

FWHM	Full-width-half-maximum
PMA	Phosphomolybdic acid
σ_e	Conductivity for electrons
σ_h	Conductivity for holes
κ_e	Chemical potential of electrons
κ_h	Chemical potential of holes
φ	electrostatic potential

SUMMARY

There is an ever-growing interest in extending the application of optoelectronic devices to biomedical applications. The seamless integration of these applications with soft materials, such as human skin, could be enabled by stretchable optoelectronics. Stretchable optoelectronics has been demonstrated either by engineering device architectures with strain-relief features or by using intrinsically stretchable semiconductors. An intrinsic stretchability of an optoelectronic device is more desirable because it could ease device fabrication and improve scalability. Organic photodiodes provide an attractive route to achieve intrinsic stretchability since optoelectrical and mechanical properties can be chemically engineered. However, the reports on stretchable organic photodiodes remain scarce.

In this work, we develop a way to accommodate stretchability on organic bulk heterojunction by blending elastomer. This work reports on the elastomeric bulk heterojunction having marginal mechanical property mismatch to human skin as well as tens of pico-watt noise equivalent power under different tensile strains.

Our approach and results demonstrate that: (1) the detailed study on photodetector characteristics allows the photodiode using the elastomeric bulk heterojunction on a rigid substrate to yield a noise equivalent power 39 pW at 653 nm. (2) With pre-strained PEDOT:PSS/PDMS as bottom electrode and substrate, the fully stretchable organic photodiode achieves noise equivalent power values in the tens of pico-watt range and an estimated average specific detectivity value of 2.3×10^{10} Jones at 653 nm up to at least 60% strain (stretchable up to possibly 100%). (3) The freestanding film of elastomeric bulk

heterojunction sustains up to 189% of tensile strain and yields Young's modulus of tens of MPa, which is comparable to human skin. These results provide a proof-of-principle that stretchable organic photodiodes can combine the unique mechanical properties of elastomers while maintaining the remarkable performance of rigid photodetectors.

CHAPTER 1. INTRODUCTION

1.1 Wearable and Biomedical Optoelectronics

For chronic illnesses such as neurological disorders, and cardiovascular disorders, the body conditions should be constantly monitored. However, these medical measurements are typically taken by visiting a hospital. This inconvenience places numerous demands on wearable electronics that can easily monitor body condition even at home, with the following properties: unobtrusive, compact, non-invasive, lightweight, simple to fabricate, and mechanically flexible. As technology evolves, the demand for interfaces that connect the digital and physical worlds continues to increase. Wearables, the internet-of-things (IoT), soft robotics, and many other emerging technologies use flexible optoelectronics to develop intelligent surfaces that combine sensors, computation, and communication. However, when objects are soft their surface deforms under stress, i.e., when they experience strain, and flexibility is no longer sufficient to ensure mechanical compliance or ergonomics. Photodetectors are an important class of sensors that generally benefit from having large photoactive areas which are sensitive to strain. Since the surface of soft objects experiences strain under normal conditions, stretchable photodetectors are expected to provide a rugged sensor platform that could find multiple applications for skin-mounted health monitors such as photoplethysmogram (PPG) sensors,^{1,2} sensors mounted on the surface of living organisms such as plants for smart agriculture, sensors for artificial skin,^{3,4} soft robotics,⁵⁻⁷ electronic eyes on curvilinear surfaces,⁸ gesture and motion recognition,⁹ among many others.

1.2 Early Development in Flexible Optoelectronics

Optoelectronic devices comprising thin films of rigid or semi-rigid materials can be engineered to be flexible and even stretchable if small rigid devices are connected through stretchable wires such as serpentine structure¹⁰⁻¹² or if thin-film devices are fabricated in pre-stretched elastomer substrates.¹³⁻¹⁶ Using these approaches, demonstrations of lightweight ultra-flexible and stretchable devices based on inorganic or organic semiconductors have been made, including thin-film transistors, photovoltaics, imaging arrays, and light-emitting diodes among many others.¹⁶⁻¹⁸ However, these strain relief features cause the complexity of the device fabrication process.

1.3 Imparting Stretchability to Organic Semiconductors

These problems can be eased by the use of organic semiconductors imparting intrinsic stretchability without heterogeneous integration. As shown in Figure 1, organic semiconductors are particularly attractive to develop soft and stretchable devices because their thermomechanical properties (e.g. a low density and tensile modulus in the range 0.1 to 1 GPa¹⁹) can be engineered through synthetic chemistry or material science approaches to mimic the properties of biological materials.

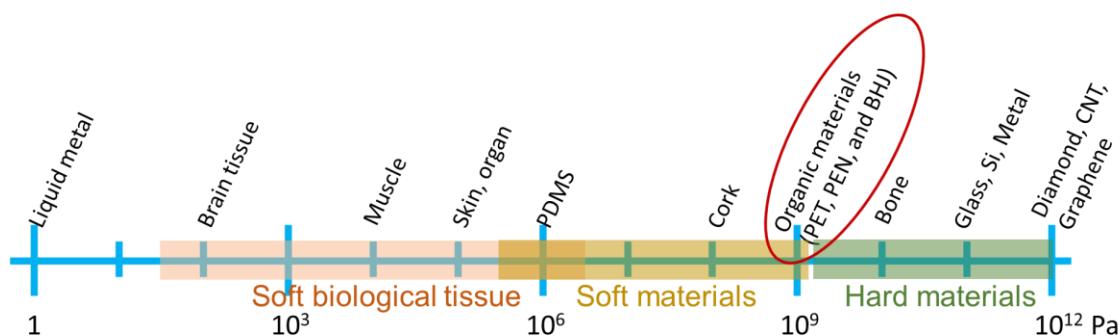


Figure 1 Young's modulus scales

Two important approaches toward intrinsic stretchability have been demonstrated. In one approach, akin to the connection of devices with stretchable wirings, molecular stretchability is engineered into conjugated polymers by adding chemical moieties to the backbone so that strain energy is easily dissipated through the amorphous regions while preserving the integrity of charge transport through more ordered regions.^{20,21} Following this approach, semiconductor polymer films and Organic field-effect transistors (OFETs)

can be stretched up to 100% strain while displaying charge mobility values ca. $0.1 \text{ cm}^2/\text{Vs}$.²⁰ In another approach, Xu, et al. showed polymer semiconductor nanofibers of high-mobility semiconducting polymers were formed through phase separation inside a soft elastomer (polystyrene-block-poly(ethylene-ranbutylene)-block-polystyrene (SEBS)) leading to the realization of highly stretchable polymer semiconductor films and stretchable OFETs that display charge mobility values in the range between 0.5 to $1 \text{ cm}^2/\text{Vs}$ when subjected to a strain of 100%.²²

1.4 Development of Organic Photodiodes (OPD)

Due to these advantages of imparting stretchability to solution-processable organic semiconductors in a relatively simple manner, OPDs that can be used in biomedical applications are attracting attention. OPDs generating photocurrent or photovoltage in response to incident light, are applicable in organic photodetectors and OPV. In 1993, Sariciftci et al. reported a diode composed of a solution-processed conjugated polymer as a donor, poly(phenylene-vinylene) (MEH-PPV), and an evaporated fullerene (C_{60}).²³ However, this bilayer structure has severe shortcomings of a short diffusion length of excitons, resulting in recombination of the excitons before reaching respective electrodes. In 1994, Heeger, et al. proposed the new concept of bulk heterojunctions (BHJ), a blend of donor and acceptor layer where consists of the interpenetration of two domains in bulk, mixed with MEH-PPV (as donors) and C_{60} (as acceptors).²⁴ The interpenetration of donor and acceptor shortens the distance excitons travel to the D/A interface while creating more donor and acceptor interfaces that promote exciton dissociation, leading to more photocurrent. Using the BHJ structure, his group reported polymeric OPDs made from poly(3-octyl thiophene) (P3OT) and MEH-PPV mixed with C_{60} , which is the first solution-processed BHJ-based OPD.²⁵ In this work, the OPDs biased at -15 V show responsivity values larger than 0.3 A/W in the visible range, which outperform commercial Si photodiodes. After that, OPDs using the BHJ structure have received numerous attention in the literature to improve their performance. Recently, the performance of optimized OPDs was found to rival that of low-noise Si photodiodes.²⁶

1.5 Recent Advances in Stretchable OPDs

Despite recent progress in the development of elastomeric semiconductors, organic photodiodes with elastomeric BHJ photoactive layers showing a small electronic noise have not been demonstrated yet. BHJ photoactive layers require a blend of π -donor- and π acceptor-like molecules forming a bulk heterojunction morphology to facilitate exciton dissociation, enable efficient photogeneration of charge carriers, and efficient carrier extraction. To date, most BHJs cannot be considered skin-like elastomers because even if some are somewhat stretchable, they have large Young's modulus (E) values in the range between ca. 200 MPa to 1 GPa,^{19,27,28} which are at least one order of magnitude larger than typical values for human tissues (< 30 MPa²⁹⁻³¹) and, with a few exceptions,^{32,33} strain at break values smaller than 10%.¹⁹

Despite showing limited mechanical properties, stretchable organic photodiodes based on these BHJs have been demonstrated in the context of photovoltaics²⁸ by using pre-strained substrates,¹³ moderately-stretchable BHJ,^{33,34} or all-polymer BHJ.^{35,36} To date, stretchable OPDs used in photovoltaics do not retain their performance under illumination beyond strain values ca. 50%, with one notable exception sustaining 100% strain but having a high E of 5.5 GPa.³³ Recently, a ternary blend of PDMS, a donor polymer, and a non-fullerene acceptor yielded a high E value of 990 MPa, maintaining a normalized power conversion efficiency (PCE) of 86.7% up to a strain of 20%.³⁷ Because these devices were tested for photovoltaic applications, their characteristics in the dark or at low irradiance values were not reported.

In the context of photodetection, stretchable OPDs have been demonstrated using conventional BHJ materials by laminating complete devices onto a pre-strained substrate. These stretchable OPDs were tested under compressive strain in the context of pulse oximetry,^{2,3} but the characterization of their performance parameters was limited to measurements of their dark current density values (in the range of 0.1-10 $\mu\text{A}/\text{cm}^2$ under reverse bias) and their responsivity ($\mathfrak{R}_{\text{max}} = 0.144 \text{ A/W}$) under 100 mW/cm^2 simulated solar illumination.²

1.6 Structure of the Dissertation

In chapter 2, the basics of semiconductor physics and organic semiconductors will be briefly reviewed. Moreover, some of the important performance metrics for stretchable organic photodiodes including the mechanical properties of thin films will be covered.

In chapter 3, the detailed experimental methods and equivalent circuit modeling will be discussed. In addition, the characterization methods for the fabricated devices will be provided.

Chapter 4 will cover the rigid photodiode with e-BHJ in detail. Based on the appropriate selection of elastomer content, the optoelectrical characteristics of OPD with e-BHJ will be introduced in a detailed manner.

Chapter 5 shows the characterization of fully stretchable OPD using e-BHJ. Using the freestanding film of e-BHJ, mechanical properties will be characterized, and it will be confirmed that e-BHJ has similar mechanical properties to those of human skin. Similar characterization methods are discussed as in chapter 4 but will be taken while stretching the device.

Chapter 6 concludes the dissertation and describes the future direction of the work. Elastomeric BHJ can be universally used such as a stretchable OPV. As mentioned in the introduction, vital signal measurement using e-OPD will be the subject of future work. In addition, replacing EGaIn with a thin hole-collecting layer makes e-OPD structure even simpler.

CHAPTER 2. ORGANIC SEMICONDUCTORS AND STRETCHABLE ORGANIC PHOTODIODES

2.1 Semiconductor Device Physics

The energy of electrons in a solid is determined by the laws of Fermi-Dirac statistics. In thermal equilibrium, the result of these statistics is the Fermi-Dirac distribution function, which provides the probability that an allowable electronic state with energy E is occupied by an electron,

$$f(E) = \frac{1}{1 + e^{(E-E_F)/kT}} \quad (1)$$

Where E_F is the Fermi level energy, T is the absolute temperature, and k is the Boltzmann constant.

The Fermi level energy is the energy for which the Fermi-Dirac occupation probability has a value of 0.5. Under thermal equilibrium, without external perturbations, such as an applied external voltage or light illumination, the Fermi level energy is spatially uniform across the semiconductor. For non-degenerate condition ($|E - E_F| > 3kT$), $f(E)$ can be approximated to the following equation:

$$f(E) \cong e^{-(E-E_F)/kT} \quad (2)$$

The Fermi level energy is also be defined by the carrier concentrations of electrons (n_0) and holes (p_0) at equilibrium as:

$$E_F = E_C + kT \ln \frac{n_0}{N_C} \quad (3)$$

$$E_F = E_V + kT \ln \frac{p_0}{N_V} \quad (4)$$

Where E_C (E_V) is the energy at the conduction (valence) band edge, N_C (N_V) is the effective density of states per unit volume in the conduction (valence) band.

For an intrinsic semiconductor, n_0 is equal to p_0 , since for every electron excited into conduction band, a vacancy or hole is left behind in the valence band. The intrinsic Fermi level energy is obtained from equations, (3) and (4).

$$E_i = \frac{E_C + E_v}{2} - \frac{kT}{2} \ln \frac{N_c}{N_v} \quad (5)$$

The intrinsic Fermi level energy is located not exactly in the center of the energy gap because of the different effective mass of electron and hole. Under non-equilibrium conditions, extra holes and electrons are generated, resulting in non-equilibrium carrier concentrations. These non-equilibrium carrier concentrations can be represented by quasi-Fermi energy levels:

$$n = n_0 + \Delta n = n_i e^{-(E_i - E_n)/kT} \quad (6)$$

$$p = p_0 + \Delta p = p_i e^{-(F_p - E_i)/kT} \quad (7)$$

Where n (p) is the total carrier concentration of electrons (holes), Δn (Δp) is the extra concentration of electrons (holes), n_i (p_i) is the intrinsic electron (hole) concentration, F_n (F_p) is the quasi-Fermi level energy for electrons (holes), and E_i is the intrinsic Fermi level energy.

The electric current is induced by charge transport through a semiconductor layer consisting of two mechanisms. The first is drift current under electric field (e.g., Induced by the difference in the work function of electrodes in organic photodiode). Free electrons are moved in the opposite direction of an electric field, governed by the following equations.

$$J_{drift,n} = qn\mu_n E \quad (8)$$

$$J_{drift,p} = qp\mu_p E \quad (9)$$

Where q is the elementary charge, μ_n (μ_p) is the mobility of electrons (holes), and E is the electric field.

The other is diffusion current by a gradient in carrier concentration. If the carrier concentration is not uniform, carriers will diffuse in the direction of the concentration gradient. This leads to an additional current contribution.

$$J_{diff,n} = qD_n \frac{dn}{dx} \quad (10)$$

$$J_{diff,p} = -qD_p \frac{dp}{dx} \quad (11)$$

Where D_n (D_p) is the electron (hole) diffusion coefficient.

Physically, both drift and diffusion are related to the random motion of carriers and their collisions in thermal equilibrium. The following equations called the Einstein relations explain the relationship between the diffusion coefficient and mobility.

$$D_n = \frac{kT}{q} \mu_n \quad (12)$$

$$D_p = \frac{kT}{q} \mu_p \quad (13)$$

The summation of drift and diffusion current leads to the total current density.

$$J_{T,n} = qn\mu_n E + qD_n \frac{dn}{dx} \quad (14)$$

$$J_{T,p} = qn\mu_p E - qD_p \frac{dp}{dx} \quad (15)$$

Evaluating the physical concepts of drift and diffusion separately, the general description where the two driving forces, the gradient in the electrostatic potential and the

chemical potential, contribute to the current, is provided. By multiplying the two driving forces by the corresponding conductivity, the current density is obtained:

$$J_n = \frac{\sigma_e}{q} (\vec{\nabla} (-q\varphi) + \vec{\nabla} \kappa_e) \quad (16)$$

$$J_p = \frac{\sigma_h}{q} (\vec{\nabla} (-q\varphi) - \vec{\nabla} \kappa_h) \quad (17)$$

Where σ_e (σ_h) is the conductivity for electrons (holes), κ_e (κ_h) is the chemical potential of electrons (holes), and φ is the electrostatic potential.

Using the relation between the electrochemical potential and quasi-Fermi level energy for electrons and holes, the total current density is:

$$F_n = \kappa_e - q\varphi \quad (18)$$

$$F_p = \kappa_h + q\varphi \quad (19)$$

$$J_T = J_n + J_p = \frac{\sigma_e}{q} \vec{\nabla} F_n + \frac{\sigma_h}{q} \vec{\nabla} F_p \quad (20)$$

Note that the total current is proportional to the conductivity and gradient in quasi-Fermi level energy for electrons and holes.

Carrier generation and recombination are important processes taking place in semiconductors, which determine the organic photodiode performance. Carrier generation is a process where electron-hole pairs are created by exciting an electron from the valence

band of the semiconductor to the conduction band, thereby creating a hole in the valence band. Recombination is the reverse process of a generation in which electrons and holes recombine and annihilate. Radiative recombination is the process by which an excited carrier is relaxed to a lower energy state, with the emission of a photon. Since radiative recombination is associated with the relaxation of excited carriers, the radiative recombination rate is proportional to the concentration of electrons in the conduction band and holes in the valence band. Auger recombination is the process in which a recombining electron transfers its energy to a secondary electron instead of emitting a photon of light. Then, the secondary excited electron is relaxed with the emission of phonons. Shockley-Read-Hall is a two-step recombination process using trap centers located within the bandgap of a material. An excited electron is relaxed down to a trap first, then annihilated by a hole to the valence band.

2.2 Organic Semiconductors

Organic semiconductors consist of organic materials based on carbon, hydrogen, and oxygen and they have semiconducting properties. Their optical and electrical properties can be controlled by modifying their chemical structure. The modification also enables the organic polymer to be soluble in organic solvents, therefore, they can be readily coated into thin films through spin-coating or directly patterned using ink-jet printing and offer unique advantages over their inorganic counterparts.

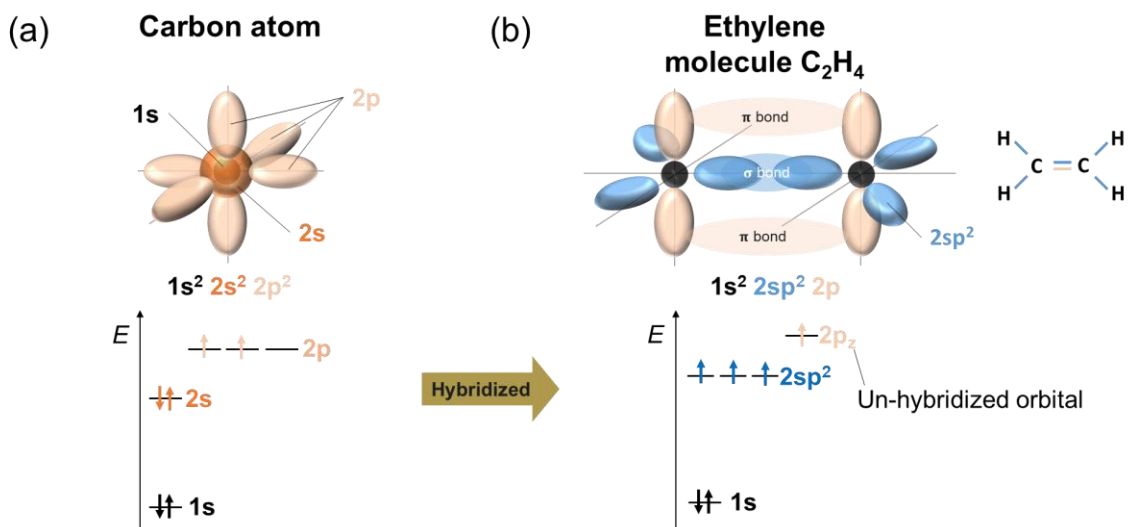


Figure 2 Orbital structures of (a) Carbon atom, (b) Ethylene molecule.

When it comes to the carbon atom, 2s and 2p orbitals are occupied by four valence electrons and lead to a configuration of $1s^2 2s^2 2p^2$. Depending on neighbor atoms, the outer-shell orbitals can be hybridized into sp , sp^2 , and sp^3 orbitals. When 2s orbital is linearly combined with all of the three 2p orbitals ($2p_x$, $2p_y$, $2p_z$), the four sp^3 hybridized orbitals

are formed, creating σ bonds with surrounding atoms. However, when a $2s$ orbital is hybridized with two $2p$ orbitals ($2p_x$, $2p_y$) leading to sp^2 hybridization, the resulting three sp^2 orbitals create σ bonding with $1s$ orbitals in the adjacent two hydrogen atoms and another sp^2 orbital in the adjacent carbon atom as shown in Figure 2 (b). The remaining unhybridized $2p_z$ orbitals form a π bond that is responsible for the double bond between carbon atoms. The electrons in the σ bond are more tightly bound to the nucleus and do not contribute to charge transport significantly. In other words, they are more localized. The electrons in the π bond are less tightly bound by the nucleus, and therefore they are relatively mobile. Under certain conditions, they can become delocalized, that is to say, they can move in the molecular skeleton from one atom to another.

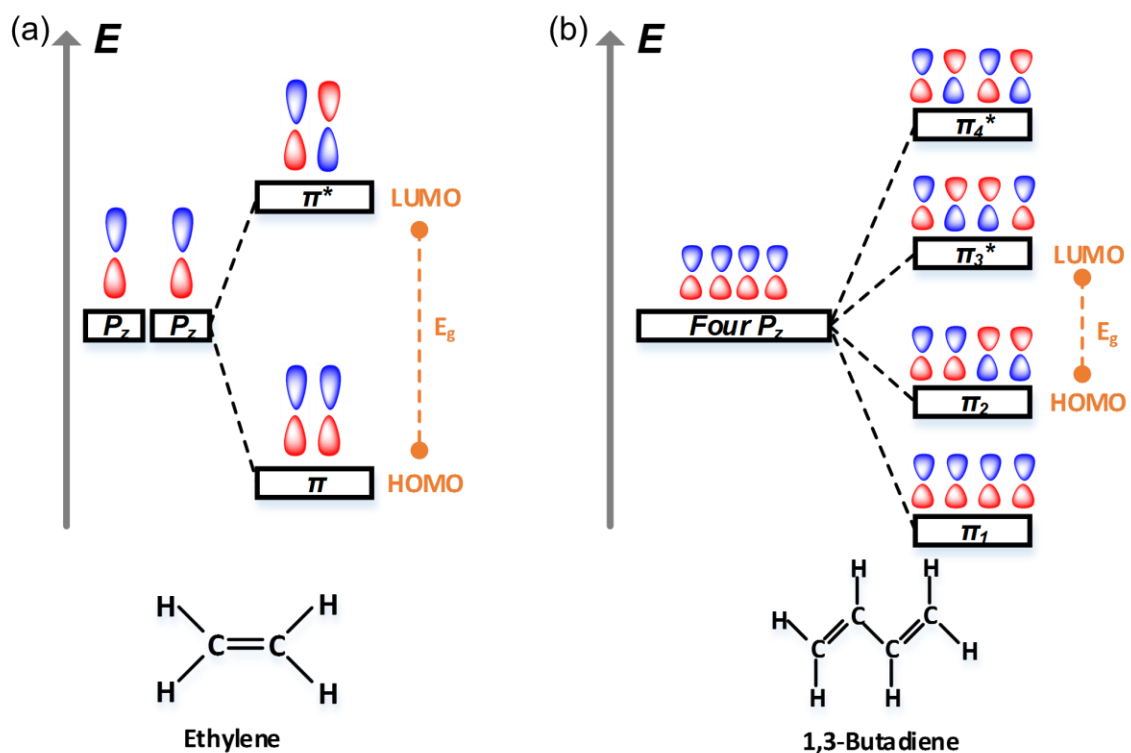


Figure 3 Energy diagram of (a) Ethylene, (b) Butadiene.

In the ethylene molecule, the linear combination of two unhybridized $2p_z$ orbitals results in the formation of two molecular orbitals, bonding orbital (π orbital) and antibonding orbital (π^* orbital). As shown in Figure 3 (a), the bonding molecular orbital is energetically favorable since its energy is lower than that of the isolated $2p_z$ orbitals. The anti-bonding molecular orbital is energetically unfavorable since the energy is higher than that of the isolated atomic orbitals. The electrons preferably stay in stable positions, which leads to forming the Highest Occupied Molecular Orbital (HOMO). The first unoccupied

energy level, π^* orbital, is called the lowest unoccupied molecular orbital (LUMO). The difference in energy between these two molecular orbitals is called the energy gap (E_g). Similarly, butadiene having more conjugation than that of ethylene provides two additional energy levels depending on the combination of molecular orbitals, resulting in narrower E_g in Figure 3 (b). The corresponding wavelength of absorption of ethylene is known to be 180 nm compared to that of butadiene, 230 nm.³⁸ If the level of conjugation is high enough, e.g., polyacetylene, the narrowed E_g leads to light absorption or emission in the visible spectral range.

Contrary to single molecules, consider a solid thin film made from a large number of molecules. Due to the manifold of intermolecular interactions in the solid and disorder, the solid can no longer be modeled by a two-level system with discrete HOMO and LUMO energies. Instead, the molecular energy levels are broadened into electronic bands which are described in terms of HOMO and LUMO bands or manifolds. In particular, the top of the HOMO band and the bottom of the LUMO band are referred to as the ionization potential (IP), the minimum energy required to create a positive charge carrier, and the electron affinity (EA), the energy gained by a negative charge carrier, respectively. The transport gap (E_{trans}) for free carriers is defined as the energy difference between the IE and the EA. The optical gap (E_{opt}) is the energy difference between the ground state and the excited state. There exists the binding energy (E_B) difference between E_{trans} and E_{opt} due to the Coulombic interaction between positive and negative charges for the exciton, which is the bound state of an electron and hole pair. The exciton binding energy is typically on the order of 0.1 - 0.5 eV for organic solids with a low dielectric constant ($\epsilon_r < 5$), much higher

than thermal energy at room temperature (0.025 eV).^{39,40} However, in inorganic semiconductors with the dielectric constant ($\epsilon_r \sim 10$), the exciton binding energy is in the order of 0.01 eV which is much lower than thermal energy at room temperature. Thus, the excitons in inorganic semiconductors are immediately dissociated into free electrons and holes by thermal energy.

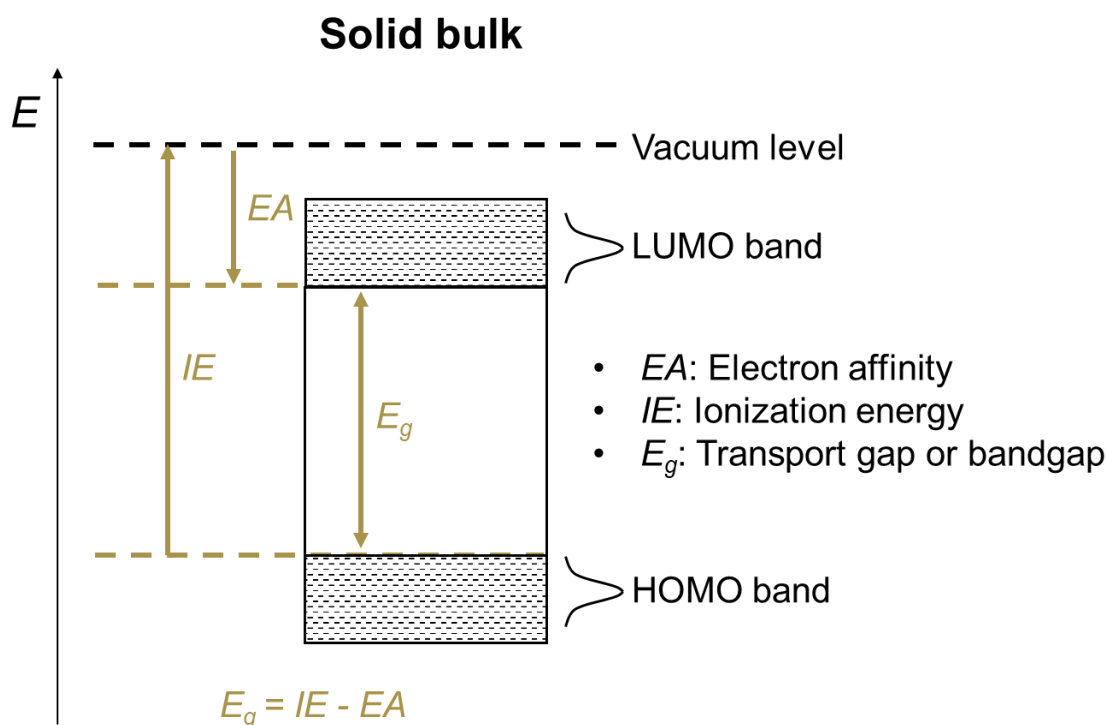


Figure 4 Energy level diagram in organic solid bulk.

In inorganic crystalline materials, the electronic wave functions are delocalized over the whole system, resulting in a band regime behavior where the charge carriers can freely move over the entire structure.⁴¹ However, in organic conjugated materials, weak

molecular interactions lead to the energy levels broadening into electronic bands with widths determined by the strength of the intermolecular interactions and disorder. Moreover, due to the weak coupling, the wave functions are localized over a few surrounding molecules. In such disordered systems, charge carriers are generally proceeded by hopping and thermal activation.⁴²

2.3 Working Principles of OPDs

2.3.1 Photoactive Layer

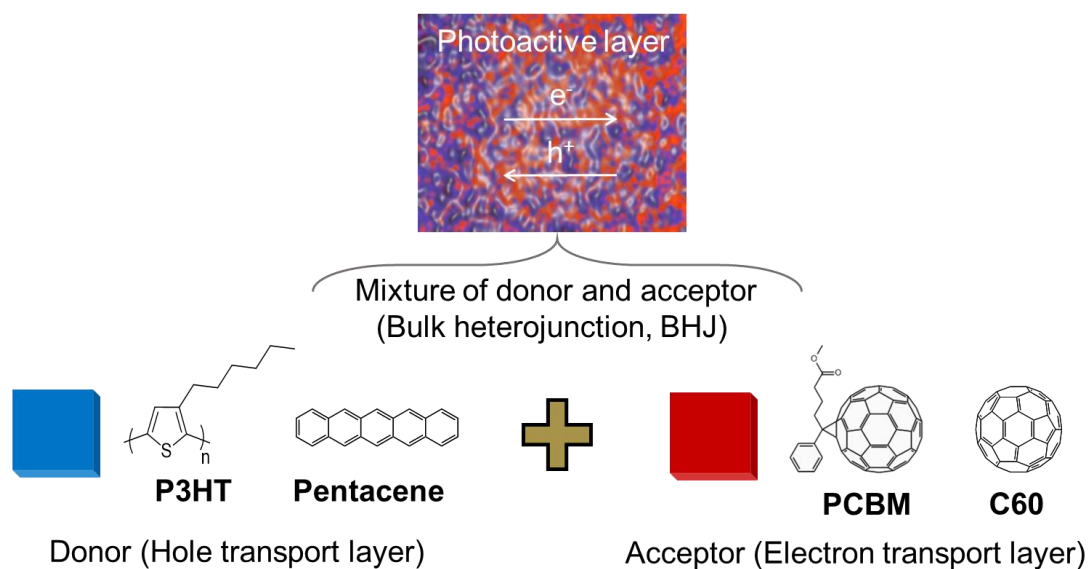


Figure 5 Schematic diagram of BHJ formation.

The photoactive layer in organic semiconductors consists of donor material with lower IE and acceptor material with higher EA and leads to the generation of excitons under the illumination of light. Since the bound excitons can acquire enough energy to be split into carriers only at the donor-acceptor interface, the combination of a donor and acceptor is required. Because early organic photodiodes had bilayers of donor and acceptor materials, due to their short exciton diffusion length (typically 10 - 20 nm), the excitons that are generated far from the donor-acceptor interface are recombined, resulting in wasted photons. Such short exciton diffusion lengths have triggered the innovative concept called bulk heterojunctions (BHJ), in which the donor and acceptor are blended and form an interpenetrating and phase-separated network with a nanoscale morphology shown in Figure 5. In this photoactive layer, the heterojunction interface can be located within the exciton diffusion length from the absorption area, and the increased interface surface areas further improve charge dissociation. At the donor-acceptor interface, the electronic coupling of each molecule results in the formation of charge-transfer states (CT) with decreased energy shown in Figure 6. The excitons with a weak Coulombically bound pair in the CT state dissociate into free charges in the presence of disorder or dipoles at the interface. The free charge carriers then move toward their favorable energy levels by a combination of diffusion and drift created by the difference in the work function of electrodes.

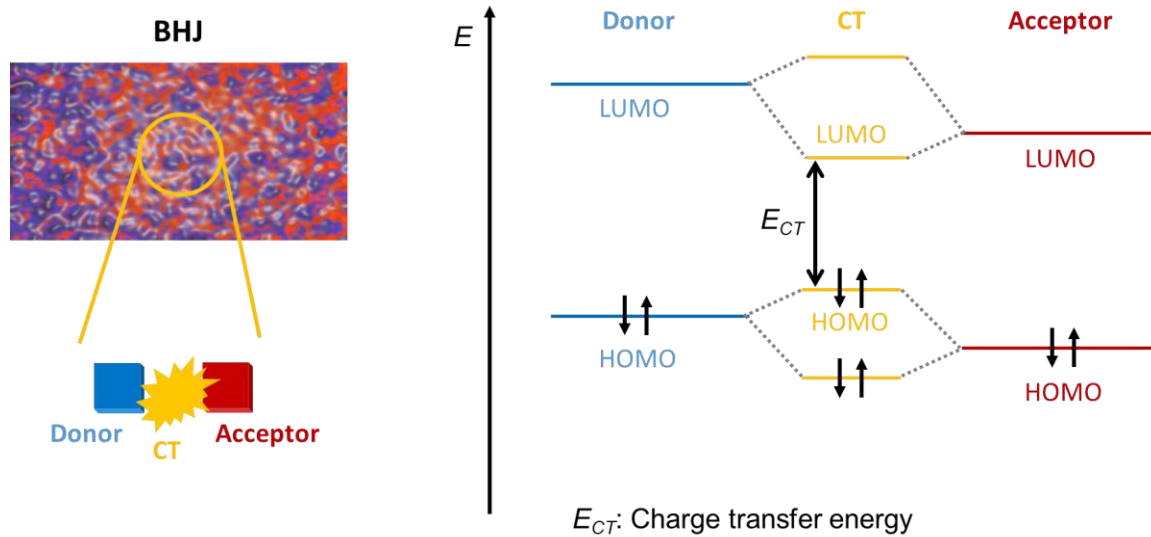


Figure 6 Schematic and energy diagram of the formation of charge-transfer states.

2.3.2 Device Structure

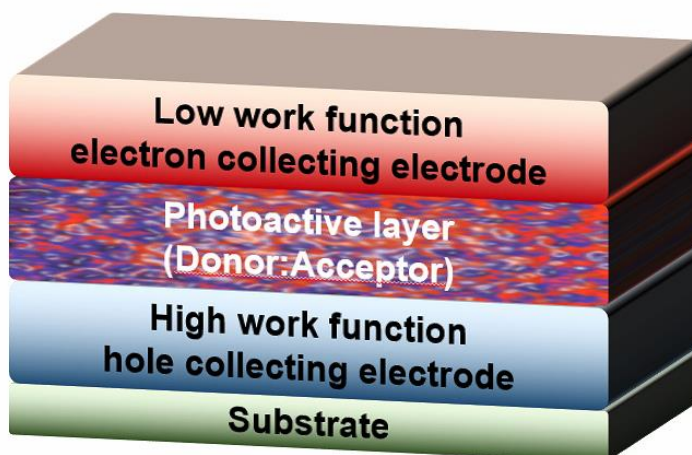


Figure 7 Device structure of OPD.

As shown in Figure 7, OPD consist of a photoactive layer, low work function electron-collecting electrode, and high work function hole-collecting electrode. One of two electrodes should be semi-transparent to allow photon penetration and absorption into the photoactive layer. To enable efficient charge collection at the electrodes, the high work function electrodes are used to collect holes from the HOMO of the donor materials, and low work function electrodes are chosen to collect electrons from the LUMO of the acceptor materials. For instance, materials with high work functions such as MoO_3 , Au, and WO_3 are good candidates for the hole-collecting layer, while materials with low work functions such as TiO_2 , ZnO , and Ca are suitable choices for the electron-collecting layer.

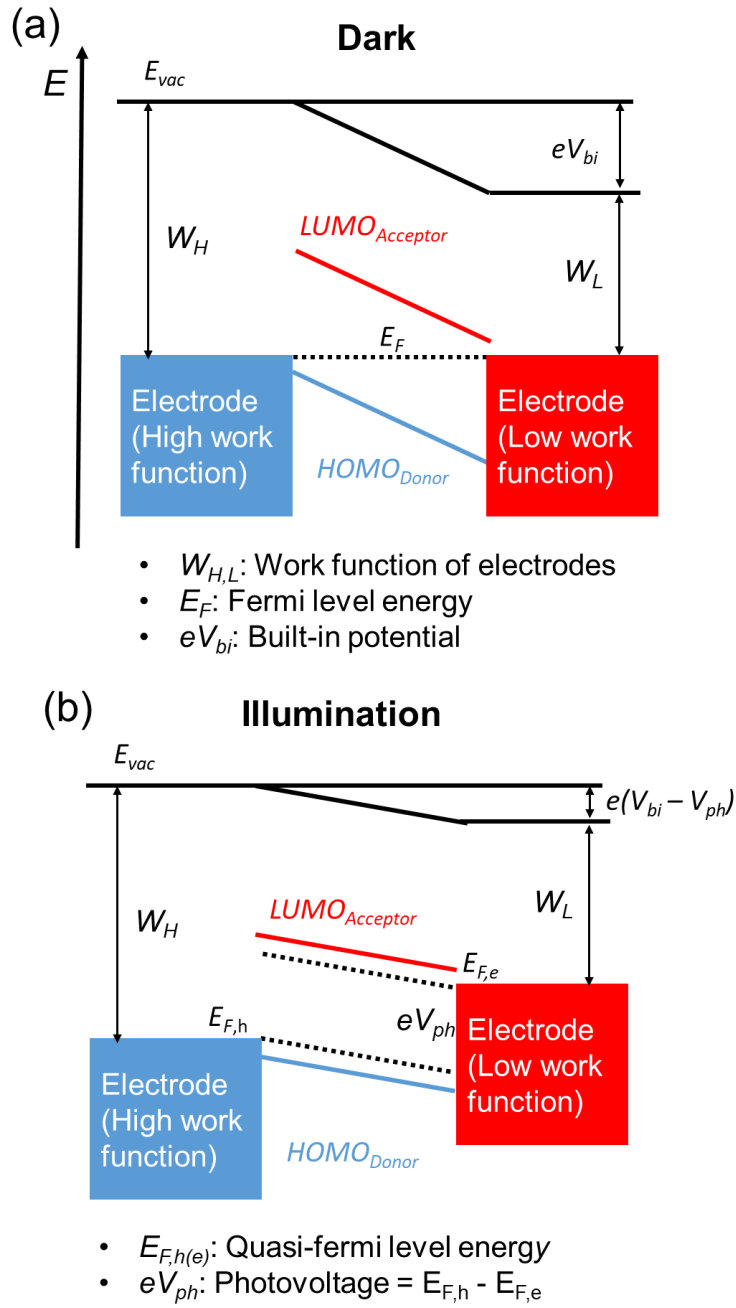


Figure 8 Energy level diagrams of OPDs under (a) Dark (b) Illumination.

Energy level diagrams of OPDs are shown in Figure 8. Under equilibrium conditions in the dark, the Fermi level energy is independent of position throughout the entire layer stack, and the difference in the work function of electrodes leads to the built-in potential. Under illumination, when the excess electrons and holes are generated in the photoactive layer, the system reaches quasi-equilibrium shown in Figure 8 (b). The gradient of the quasi-Fermi level energies leads to photocurrents and the differences in quasi-Fermi level energies at electrodes provide photovoltage (V_{ph}).

2.4 Performance Metrics of Stretchable OPDs

2.4.1 Responsivity

The responsivity (\mathfrak{R}) is the ratio of the generated photocurrent (I_{ph}) to the incident optical power (P_{in}). External Quantum Efficiency (EQE) is the ratio of the number of charge carriers collected to the number of incident photons. Since optical power is proportional to the number of photons and the energy of photons, the corresponding equations follow:

$$\mathfrak{R}(\lambda) = \frac{I_{ph}}{P_{in}}, \quad EQE(\lambda) = \frac{hc}{\lambda q} \mathfrak{R}(\lambda) \quad (21)$$

Where λ is the wavelength, h is the Planck constant, c is the speed of light, and q is the elementary charge.

2.4.2 Noise

In the context of a photodetector, suppressing noise allows for low-power optical signal detection. Shot noise (S_{shot}) is associated with a discrete structure of electricity and the individual carrier injection across the interfaces.⁴³ Thermal noise ($S_{thermal}$) is created by the random motion of charges due to thermal excitation, which depends on temperature and shunt resistance. $1/f$ noise ($S_{1/f}$) is a low-frequency noise with a noise power that is inversely proportional to the frequency. The origin of $1/f$ noise at low frequencies has not

been well understood until now.⁴⁴ Since the noises mentioned above are independent of each other, the total noise power spectral density (S_n) is described by the following equation (22).

$$S_n = S_{shot} + S_{thermal} + S_{1/f} = 2q \left[J_0 \exp\left(\frac{qV}{nkT}\right) A + J_0 A \right] + \frac{4kT}{R_p} + i_{1/f}^2(f) \quad (22)$$

Where q is the electron charge, k is the Boltzmann constant, J_0 is the reverse saturation current, T is the absolute temperature, R_p is the shunt resistance of OPD, A is the device area, and $i_{1/f}$ is the $1/f$ noise term.

2.4.3 Noise Equivalent Power and Specific detectivity

In order to quantify the noise of the photodetectors, a root-mean-squared electronic noise current (I_{rms}) is derived by calculating the square root of the mean square of the current residuals derived from estimating the average current over time by fitting the current transients to an exponential decay function shown in Figure 9. The square root of the integration of S_n over the measurement bandwidth (B) leads to I_{rms} , expressed in equation (23).

$$I_{rms} = \sqrt{\int_B S_n(f) df} \quad (23)$$

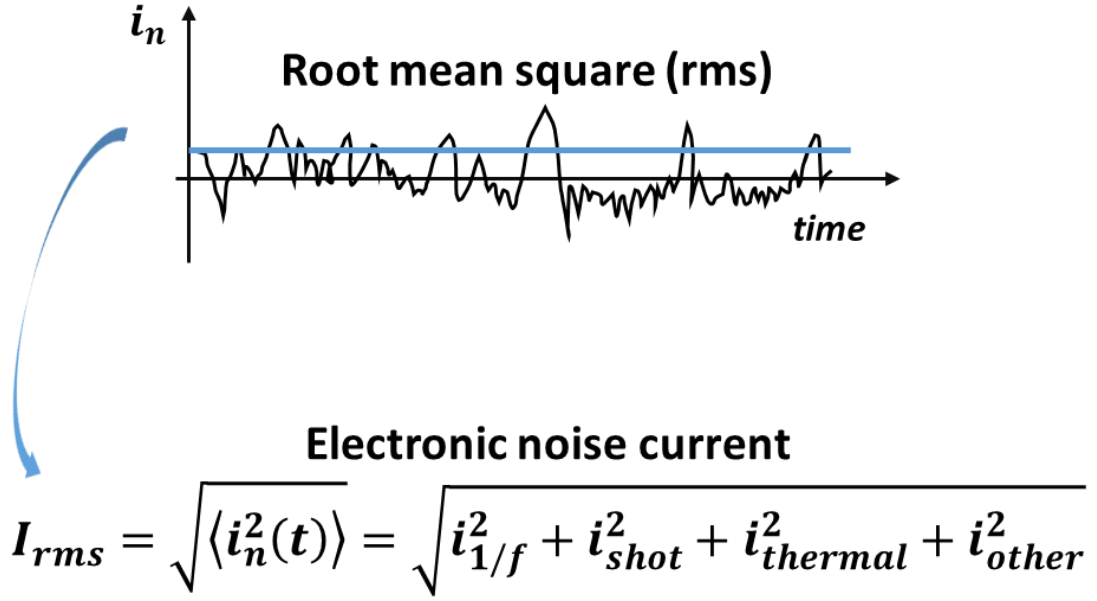


Figure 9 Derivation of electronic noise current from rms current.

An important figure of merit of photodetectors is the noise equivalent power (NEP), defined as the incident optical power required to generate the photocurrent equal to the electronic noise current, shown in equation (24).

$$NEP = \frac{I_{rms}}{\Re} \quad (24)$$

The Specific detectivity (D^*) is used to compare detection capacities between different photodetectors, obtained by normalizing the inverse of NEP with respect to the device area and the measurement bandwidth expressed in (25).

$$D^* = \frac{\sqrt{AB}}{NEP} \quad (25)$$

2.4.4 Response Time

When a pulsed source of light is illuminated on photodetectors, the response time is considered as either the rise time or fall time required for the output current to go from 10% to 90% of its steady-state on-current shown in Figure 10. The response time for collection of each carrier to electrodes is primarily dependent on the field-dependent carrier transit time (τ_{drift}), the diffusion time before recombination (τ_{diff}), and the RC time delay associated with effects of the external circuit (τ_{RC}). The total response time is expressed in (26)

$$t = \sqrt{\tau_{\text{drift}}^2 + \tau_{\text{diff}}^2 + \tau_{\text{RC}}^2} \quad (26)$$

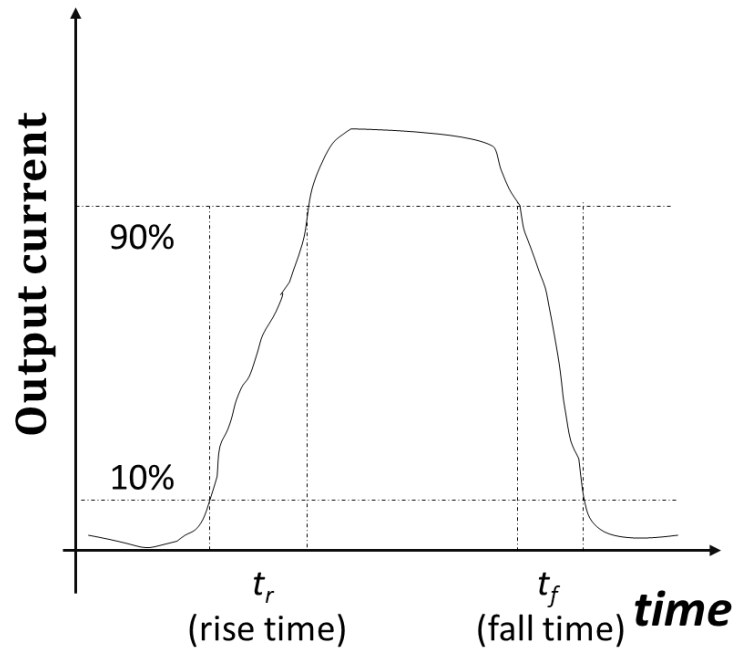


Figure 10 The response time measurement.

2.4.5 Mechanical Properties of Films

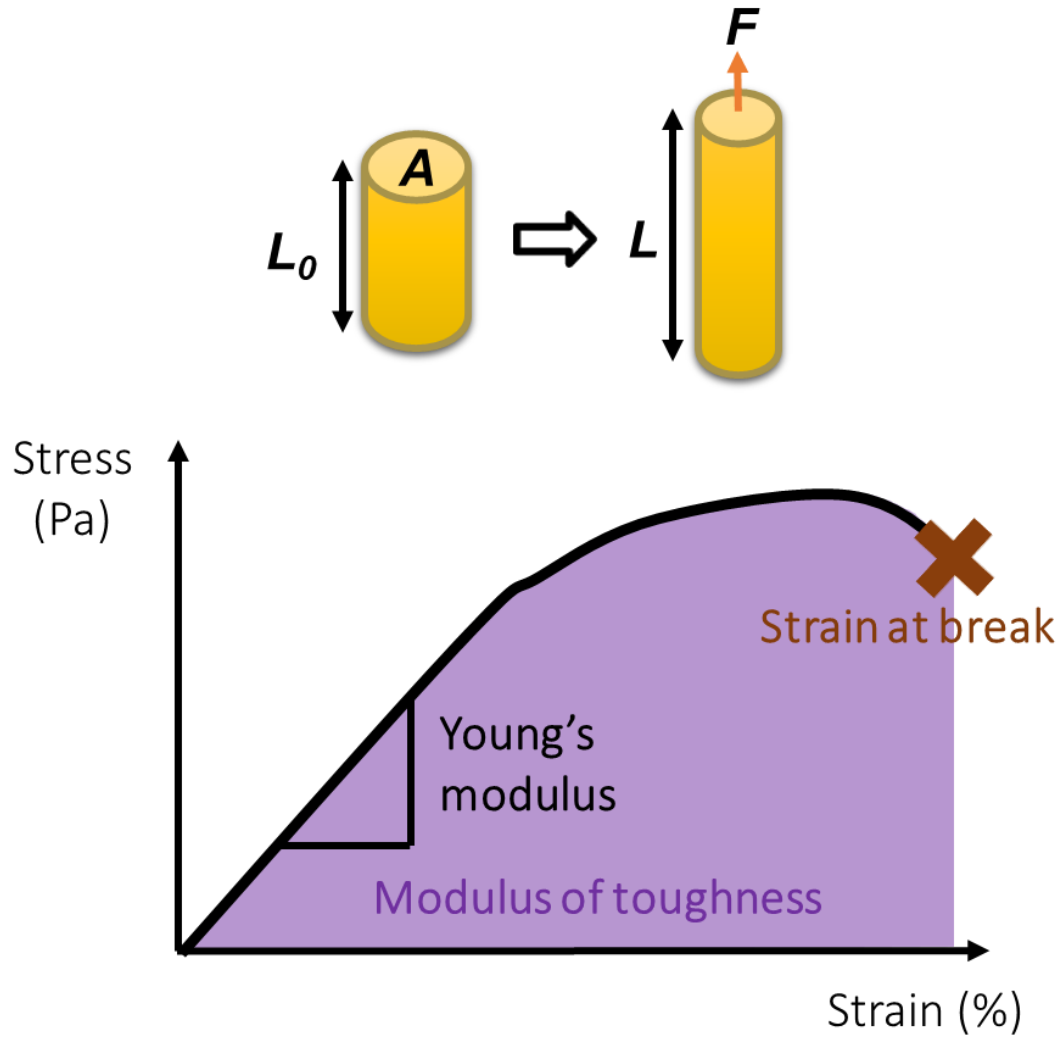


Figure 11 Tensile test diagram and curve.

Figure 11 shows a tensile test diagram and curve. Stress is defined as the force per unit area of a material. A strain is defined as an extension per unit length. Tensile modulus is defined as the slope of its stress-strain curve in the elastic region, which is a measure of the ability of a solid material to withstand changes in length and describes the elastic

properties of the material. Modulus of toughness is the amount of strain energy per unit volume that a material can absorb before rupturing and is calculated by using the area underneath the stress-strain curve.

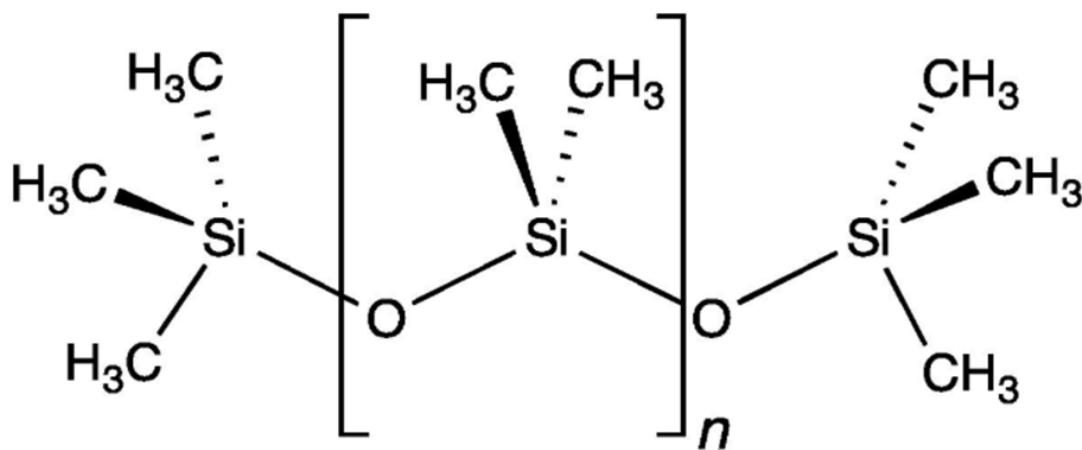
$$\sigma = \frac{F}{A}, \quad \varepsilon = \frac{l - l_0}{l_0}, \quad E = \frac{\sigma}{\varepsilon} \quad (27)$$

Where σ is the stress, F is the force applied, A is the cross-sectional area of the material, ε is the strain, l is the stretched length, l_0 is the original length, and E is Young's modulus.

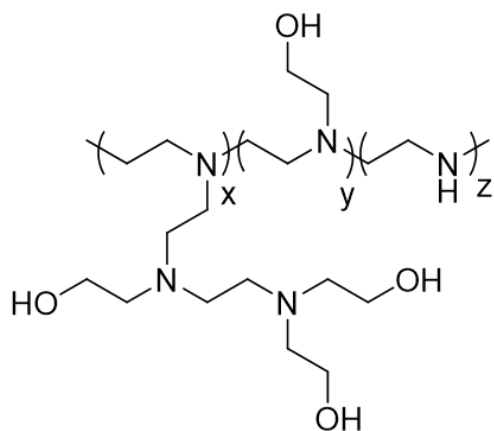
CHAPTER 3. EXPERIMENTAL METHODS AND MODELING

3.1 Materials

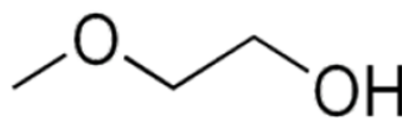
Glass and polydimethylsiloxane (PDMS) (Dow Corning Co., Sylgard 184) were used as substrates. Custom-patterned Indium-doped tin oxide (ITO) and poly(3,4-ethylenedioxythiophene):polystyrene sulfonate (PEDOT:PSS) (Ossila) were used as bottom electrodes. For electron-collection layer, polyethylenimine-ethoxylated (PEIE) (Sigma Aldrich) diluted in 2-methoxyethanol (Sigma Aldrich) were used for work function reducing interlayer for bottom electrodes. Eutectic Gallium-Indium (EGaIn) (Sigma Aldrich) was used for top electrodes as an electron collection layer. The bulk heterojunction consists of poly(3-hexylthiophene-2,5-diyl) (P3HT) (Rieke Metals) as donor materials and indene C₆₀-bisadduct (ICBA) (Nano-C), [6,6]-Phenyl C₆₁ butyric acid methyl ester (PCBM) (Nano-C) as small molecule fullerene acceptors. The solvent used to dissolve the BHJ was chlorobenzene (Sigma Aldrich). For hole-collection layers, a thermally evaporated layer of MoO₃ was used on top of photoactive layers. The elastomer SEBS (Asahi Kasei Corporation) was mixed with BHJ to impart stretchability. The chemical structure of these materials is shown in Figure 12.



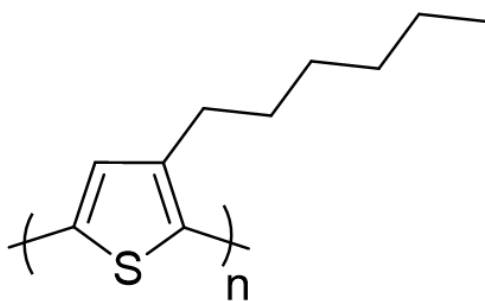
PDMS



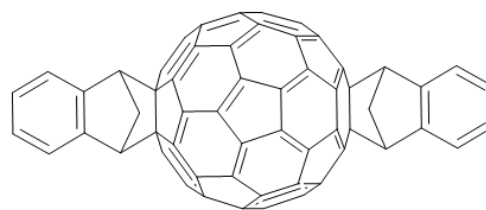
PEIE



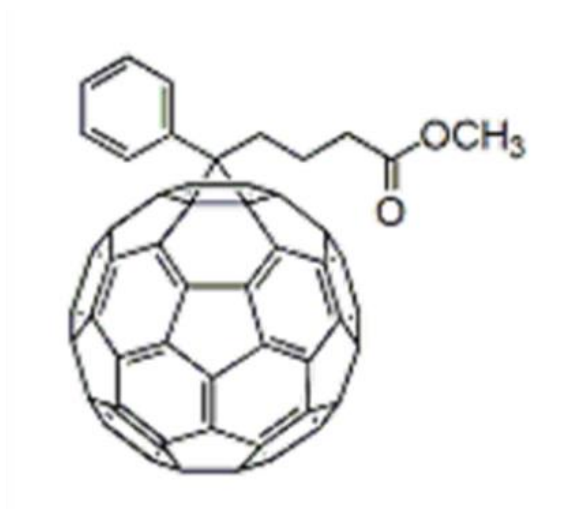
2-methoxyethanol



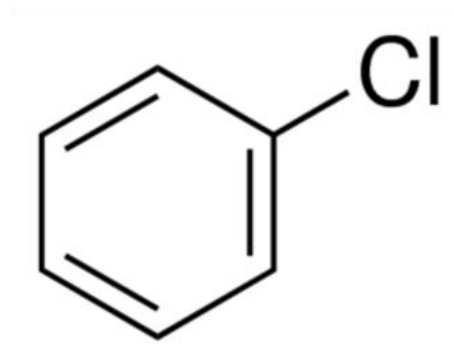
P3HT



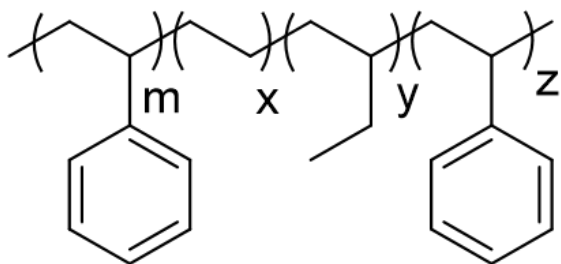
ICBA



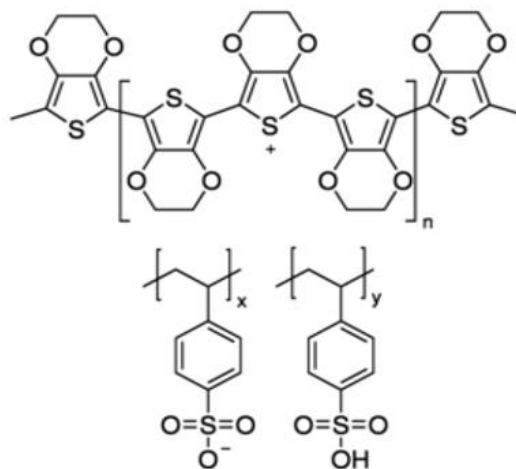
PCBM



Chlorobenzene



SEBS



PEDOT:PSS

Figure 12 Chemical structure of materials

3.2 Fabrication

Samples of SEBS:P3HT:ICBA with different compositions were initially prepared and evaluated in a photodiode device architecture in section 4.2.1. Based on the preliminary screening of their optical and electrical properties, films with a SEBS:P3HT:ICBA (2:1:1 by weight) composition were found to yield the best performance. Hence, films with a SEBS:P3HT:ICBA (2:1:1 by weight) composition, hereon referred to as e-BHJ, were characterized and compared with those of P3HT:ICBA (1:1 by weight), hereon referred to as r-BHJ.

3.2.1 Fabrication of Freestanding Films

Glass substrates were cleaned in sequential ultrasonic baths of Liquinox detergent in deionized water, deionized water, acetone, and isopropanol. To create a sacrificial layer, PEIE dissolved in H₂O at a concentration of 37 wt.% was further diluted with 2-methoxyethanol to a concentration of 18 wt.%. This PEIE solution was then spin-coated on a cleaned glass substrate at 1000 rpm for 1 min and annealed on a hot plate at 100 °C for 10 min. The PEIE-coated substrate was then transferred into an N₂-filled glove box for further processing. The r-BHJ and e-BHJ consist of a blend of regioregular P3HT with ICBA at a 1:1 weight ratio and a blend of SEBS:P3HT:ICBA at a 2:1:1 weight ratio, respectively. Chlorobenzene solutions of the r-BHJ, e-BHJ, and pristine SEBS at a concentration of 80 mg/mL were stirred overnight at 70 °C on a hotplate in the nitrogen-filled glovebox and cooled down at room temperature before they were spin-coated onto

the Glass/ITO/PEIE substrate at 800 rpm for 30 s. The resulting wet films were then slowly dried inside covered glass Petri dishes for 3 h. The sample was then thermally annealed on a hot plate at 150 °C for 10 min. The thicknesses of the r-BHJ, e-BHJ, and SEBS freestanding films are 700 ± 2 nm, 1000 ± 8 nm, and 1683 ± 9 nm, respectively, measured with a scan area of $30 \mu\text{m} \times 30 \mu\text{m}$ by Atomic Force Microscopy (AFM). Each film was cut into an $8 \text{ mm} \times 38 \text{ mm}$ strip, and each end of the film was gently pressed on the PDMS for van der Waals bonding to allow tensile testing. The freestanding films in the form of a strap were obtained by immersing the substrate in deionized water for 30 min to completely dissolve the PEIE underneath.

3.2.2 Fabrication of Rigid Photodiodes with elastomeric BHJ (e-BHJ)

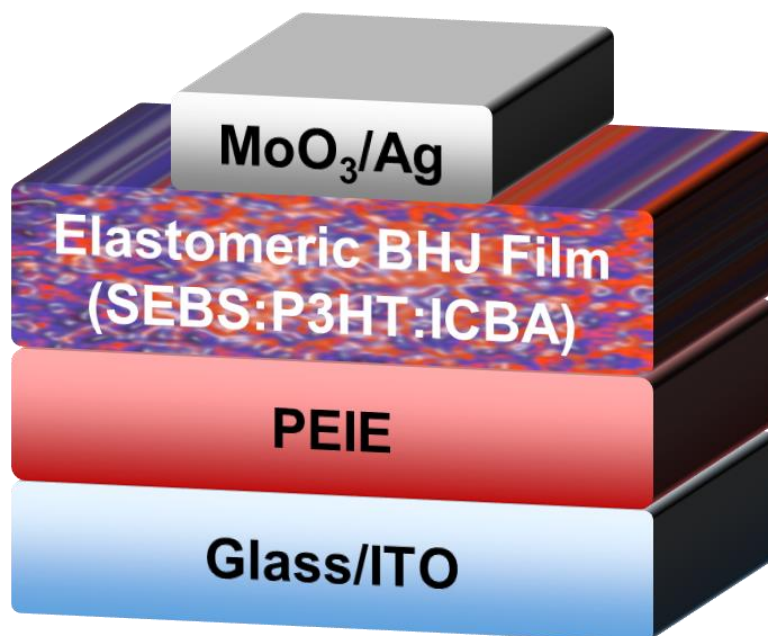


Figure 13 The device structure of elastomeric OPD.

Figure 13 shows the device structure of elastomeric OPD with e-BHJ on a rigid substrate. the BHJ of our photodiode uses a blend of regioregular SEBS:P3HT:ICBA as a photoactive layer, PEIE⁴⁵ is used to reduce the work function of ITO allowing it to act as an electron collecting electrode. MoO₃/Ag is used at the top as a hole-collecting electrode. Custom-patterned ITO-coated glass sheets with a sheet resistance of 12-15 Ω /sq. were used as a substrate for OPDs. The ITO substrate was cleaned in ultrasonic baths of Liquinox detergent in deionized water, deionized water, acetone, and isopropanol sequentially. PEIE dissolved in H₂O at a concentration of 37 wt.% was further diluted with 2-methoxyethanol to a concentration of 0.3 wt.%. The 0.3 wt.% PEIE solution was then spin-coated on the ITO substrate at 5000 rpm for 1 min and annealed on a hot plate at 100 °C for 10 min. The substrate was then transferred into an N₂-filled glove box for further processing. The r-BHJ consists of a blend of regioregular P3HT with ICBA at a 1:1 weight ratio. Elastomeric BHJ consists of P3HT:ICBA at a 1:1 weight ratio and SEBS at different weight ratios (e.g. 30%, 50% and 67%) with respect to P3HT:ICBA. A chlorobenzene solution of the e-BHJ at a concentration of 40 mg/mL was stirred overnight at 70 °C on a hotplate in the nitrogen-filled glovebox and cooled down at room temperature before they were spin-coated onto the Glass/ITO/PEIE substrate at 800 rpm for 30 s. The resulting wet films were then slowly dried in covered glass Petri dishes for 3 h. The sample was then thermally annealed on a hot plate at 150 °C for 10 min. The thickness of the e-BHJ is 400 ± 8 nm measured with a scan area of $30 \mu\text{m} \times 30 \mu\text{m}$ by AFM. To provide effective hole collection MoO₃/Ag

(20/150 nm) was deposited on top of the substrate through a shadow mask with an effective area (A_{PD}) of 0.1 cm^2 at a pressure of $< 5.0 \times 10^{-7} \text{ Torr}$.

3.2.3 Fabrication of elastomeric OPD (e-OPD)

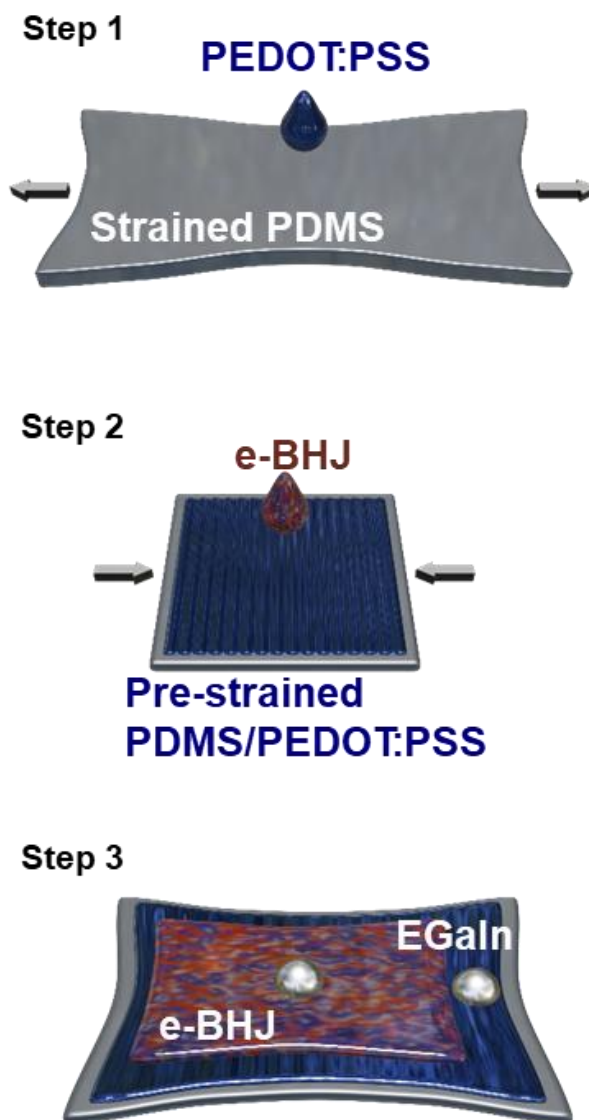


Figure 14 Schematics of the fabrication process of e-OPD.

Silicone elastomer PDMS was used as an elastomeric substrate for e-OPD. A sheet of PDMS (2 - 3 mm thick) with a curing agent/base ratio of 1:20 was obtained by curing in an oven at 60 °C for 3 h. Strained PDMS sheets (30%, 60%) were fixed on glass with paper clips. PEDOT:PSS (Ossila, PH 1000) with 12 wt.% of ethylene glycol and 15 wt.% of Capstone was spin-coated on the strained PDMS at 1000 rpm for 1 min and annealed on a hot plate at 100 °C for 10 min. The thickness of the PEDOT:PSS deposited on glass is 392 ± 6 nm measured at three different spots by a profilometer. After releasing, by removing the paper clips from glass, the substrate was transferred into an N₂-filled glove box for further processing. A chlorobenzene solution of the e-BHJ with a concentration of 40 mg/mL was stirred overnight at 70 °C on a hotplate in the nitrogen-filled glovebox and cooled down at room temperature before it was spin-coated onto the pre-strained PDMS/PEDOT:PSS at 800 rpm for 30 s. The resulting wet film was then slowly dried in a covered glass Petri dish for 3 h. The device was completed by placing a liquid metal alloy, EGaIn, on top of e-BHJ through a PDMS mask to control the area.

3.3 Characterization

3.3.1 Photodetector Characterization

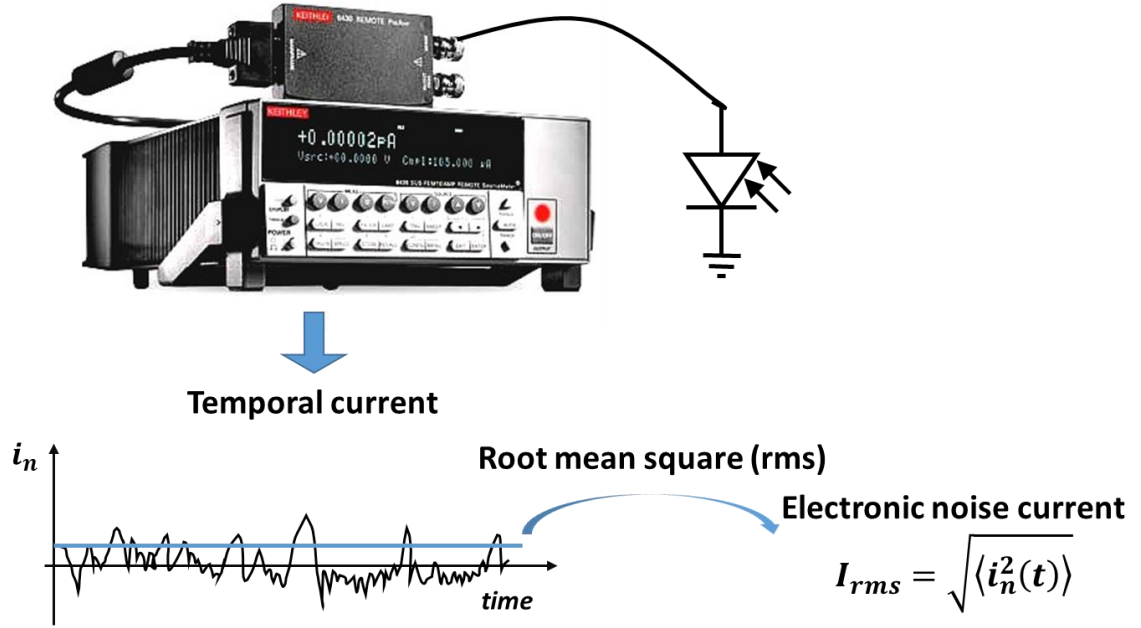


Figure 15 Schematic of extracting rms electronic noise current measurement

The dark current and electronic noise were measured using a Keithley 6430 electrometer shown in Figure 15. The current was recorded as a function of time using a LabView program. The voltage was controlled manually to allow for the dark current to reach steady-state values. The root-mean-squared electronic noise current was derived by calculating the square root of the mean square of the current residuals derived from estimating the average current over time by fitting the current transients to an exponential

decay function. The effective bandwidth of these measurements was estimated to be 1.5 Hz by measuring the current-voltage characteristics and electronic noise of a 1 G Ω resistor.

Similarly, the transient current was measured by the same procedure outlined above to ensure the measurement of steady-state values. The photocurrent extracted by subtracting the fitted dark current from the measured transient current was generated as a function of optical power (laser diode with a wavelength of 653 nm) by changing the bias voltage on the laser diode. The NEP and D^* are defined as the optical power producing a signal-to-noise ratio ($SNR = I_{ph}/I_{rms}$) of one and $\sqrt{A_{PD}B}/NEP$, respectively.

The spectral responsivity $\mathcal{R}(\lambda)$ was measured by using a laser-driven light source (Energetiq EQ-99X) connected with a monochromator (CVI Spectral Products, CM110) to produce spectrally narrow (ca. 10 nm full-width-half-maximum, FWHM) illumination. The light source was collimated using an optical lens and illuminated onto the device. Optical band-pass filters were placed in front of the beam path to avoid multiple frequency harmonics. The optical power was calibrated using Si photodiode (Hamamatsu S2386-44K) and a power meter (OPHIR, PD300R-UV-SH-ROHS). The steady-state current at each wavelength was measured using the same electrometer and procedure previously described. The responsivity values were derived from the photocurrent measured at each wavelength divided by the optical power.

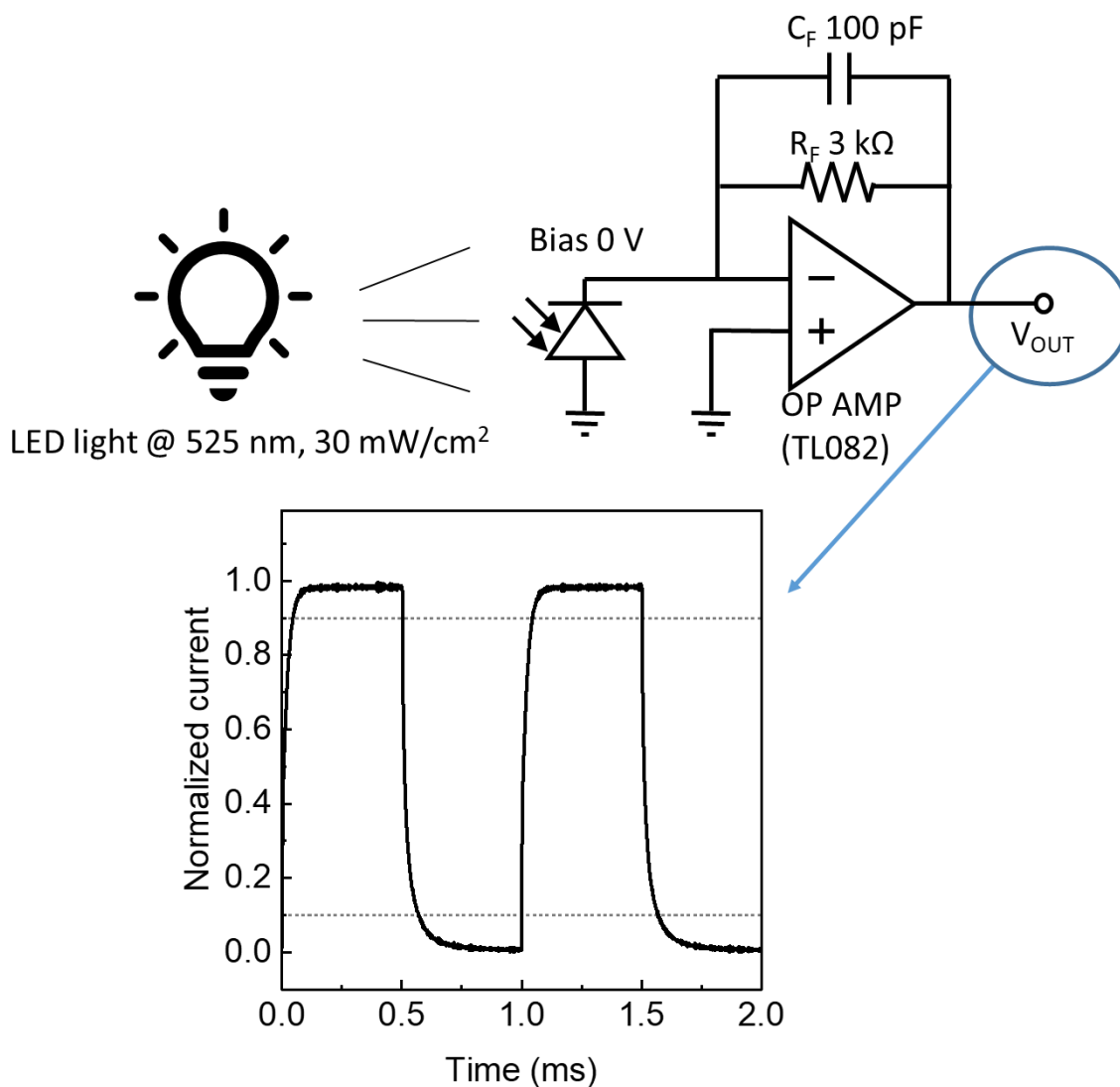


Figure 16 Schematic of response time measurement.

The response time and frequency response of the e-OPD were measured using transimpedance amplifier shown in Figure 16. The photodetector current in response to light square pulse with a green LED at 525 nm of wavelength with an irradiance of 30 mW cm⁻² was passed through a transimpedance amplifier designed by an operational amplifier

(Texas Instruments, TL082), feedback resistance of 3 k Ω , and capacitance of 100 pF. The output voltage was obtained by an oscilloscope (Rohde&Schwarz, RTO 1002). We define the rise time as response time, it takes for the output signal to go from 10% to 90% of its steady-state on-current. The transient voltage amplitude of e-OPD at each frequency was normalized to the amplitude measured at 10 Hz by sweeping the LED light frequency to obtain normalized responsivity.

3.3.2 Mechanical Characterization

The mechanical properties of the r-BHJ, e-BHJ, and SEBS were determined in a portable tensile stage (TST-350, Linkam Scientific). A uniaxial monotonic loading was applied to the film on the surface of the water at a rate of 0.5 %/s until failure occurred in the middle of the specimen. A custom-made mini water reservoir was used to float the film. A gauge length was calculated for the freestanding film between the two PDMS holders. The engineering stress, σ_{eng} , and strain, ε_{eng} , were obtained based only on the initial cross-section area, A_0 , and gauge length, L_0 , as:

$$\sigma_{eng} = \frac{F}{A_0} \quad (28)$$

$$\varepsilon_{eng} = \frac{L - L_0}{L_0} \quad (29)$$

where F is the load measured, and L is the elongated gauge length. The true stress, σ_{true} , and strain, ε_{true} , were derived based on the instantaneous cross-sectional area, A , at the gauge length L assuming that the volume of the film was preserved with Poisson's ratio of 0.5. The correlation between true stress-strain and engineering stress-strain can also be found. Therefore,

$$\sigma_{true} = \frac{F}{A} = \frac{F L}{A_0 L_0} = \sigma_{eng}(1 + \varepsilon_{eng}) \quad (30)$$

$$\varepsilon_{true} = \ln\left(\frac{L}{L_0}\right) = \ln(1 + \varepsilon_{eng}) \quad (31)$$

3.4 Equivalent Circuit Model

An equivalent circuit model of a photodiode is the form of a theoretical circuit based on the electrical characteristics under dark and light conditions. Figure 17 (a) shows the equivalent circuit composed of a diode, a current source (J_{ph}), a series resistance (R_s), and a shunt resistance (R_p). The diode explains a current rectification property with a reverse saturation current density of J_o and an ideality factor of n . The current source provides the photocurrent generated by light. The series resistance corresponds to the parasitic resistance of the photodiode caused by the contact resistance and the resistance from external interconnections. The shunt resistance is associated with possible leakage paths that arise from defects in bulk, such as pinholes and thin-thickness of the photoactive layer. Typical J - V characteristics of a photodiode are shown in Figure 17 (b). Based on the description by Prince, The current-voltage relationship of this circuit is solved as the following equations:^{43,44}

$$J = \frac{1}{1 + R_s/R_p} \left[J_o \left\{ \exp \left(\frac{V - JR_s A}{nV_T} \right) - 1 \right\} - \left(J_{ph} - \frac{V}{RPA} \right) \right] \quad (32)$$

Where V_T is thermal energy divided by elementary charge.

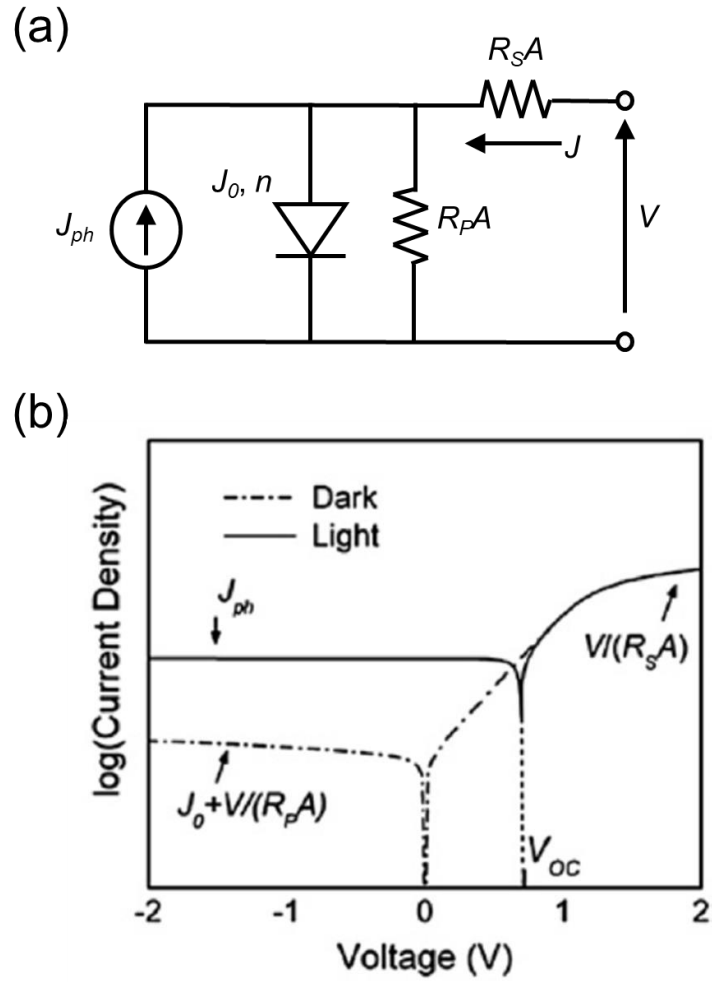


Figure 17 (a) Equivalent circuit model of a photodiode. (b) J-V characteristics of Equivalent circuit model

CHAPTER 4. RIGID PHOTODIODES WITH ELASTOMERIC BULKHETEROJUNCTION

4.1 Introduction

As briefly shown in 3.2.2, the OPD was fabricated using a blend of the elastomer SEBS, the donor polymer P3HT, and the acceptor ICBA as a photoactive layer on a rigid substrate to evaluate various photodetector characteristics. Thanks to the elastomer, the dark current was reduced by four orders of magnitude, which is consistent with higher shunt resistance than the OPD without elastomer. Additionally, electronic noise for OPD with e-BHJ is comparable to that of low-noise SiPDs (Hamamatsu S1133 series) and state-of-the-art P3HT:ICBA OPDs recently reported.²⁶

4.2 Optoelectrical Characteristics of Rigid Photodiodes with e-BHJ

4.2.1 Optimization of SEBS Contents

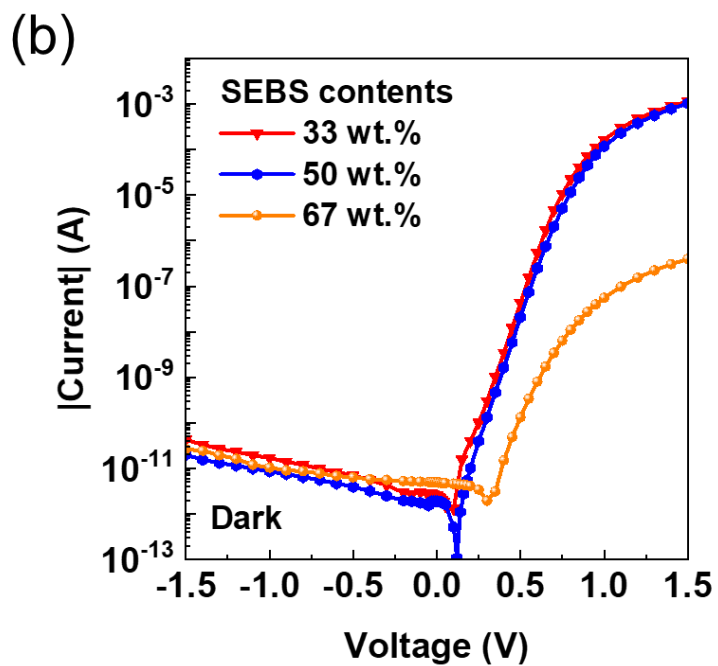
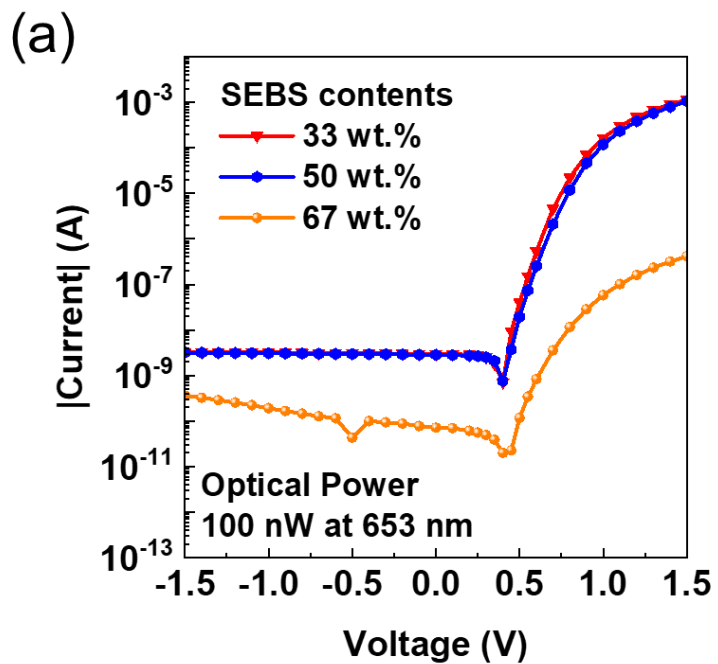


Figure 18 *I-V* characteristics of OPDs with SEBS contents of 33 wt.%, 50 wt.%, and 67 wt.%, respectively, (a) measured with an optical power of 100 nW at 653 nm, (b) measured under dark.

To determine the optimum content of a SEBS, the OPDs with e-BHJ were fabricated on a rigid substrate as detailed in section 3.2.2. We rapidly investigated the responsivity at a bias of 0 V with an optical power of 100 nW at 653 nm for OPDs with BHJs comprised of a blend of P3HT:ICBA:SEBS with SEBS contents of 33 wt.%, 50 wt.%, and 67 wt.%. Figure 18 (a) shows that the device with 33 wt.% yields a responsivity of 28 mA/W. The OPD with SEBS content of 50 wt.% exhibits a responsivity of 27 mA/W, which is relatively a small difference, 1 mA/W. However, The OPD with 67 wt.% exhibits a responsivity of 0.5 mA/W, which is significantly lower than those of the other SEBS compositions (33 and 50 wt.%). Therefore, we will primarily characterize the OPD with SEBS content of 50 wt.% referred to as e-BHJ. Figure 18 (b) shows that all of *I-V* characteristics of the OPDs under dark remain similar dark current level.

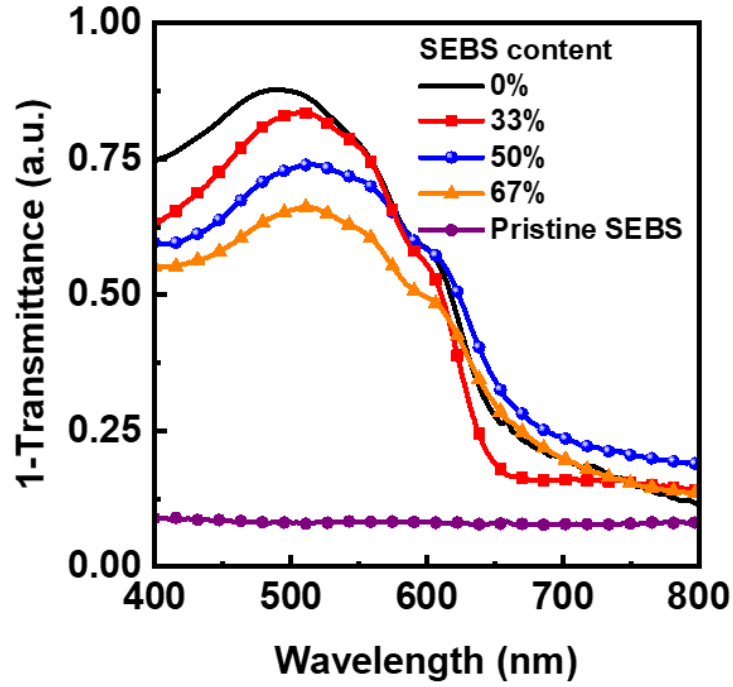


Figure 19 Spectral absorption (1-transmittance) of BHJs on glass

Figure 19 shows the spectral absorption estimated by 1-transmittance of OPDs spin-coated on glass. As SEBS contents increases, less light is absorbed. However, this result is not consistent with the similar responsivity of the ones with 33 wt.% and 50 wt.% while that of 67 wt.% significantly dropped. More in depth-studies are needed to fully understand the cause of this phenomenon.

4.2.2 Equivalent Circuit Analysis

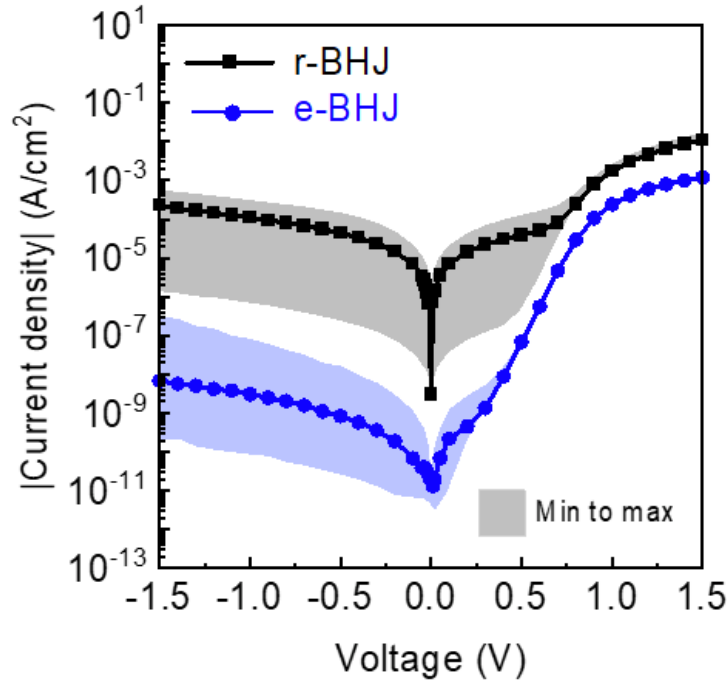


Figure 20 Comparison of the dark current density of OPDs measured in the dark. The shaded area represents the range from maximum to minimum dark current density values for samples of the same structure.

Figure 20 shows a comparison of the dark current density characteristics for OPDs having e-BHJ and r-BHJ with average thickness values of 400 nm and 260 nm, respectively, obtained by AFM. The solid lines in Figure 20 reveal that the median dark current density in OPDs with an e-BHJ is about four orders of magnitude smaller than those in OPDs with r-BHJ. While both types of devices display a large device-to-device variability (represented by the shaded areas), these results clearly show that OPDs with e-BHJ can achieve a reduction in dark current values.

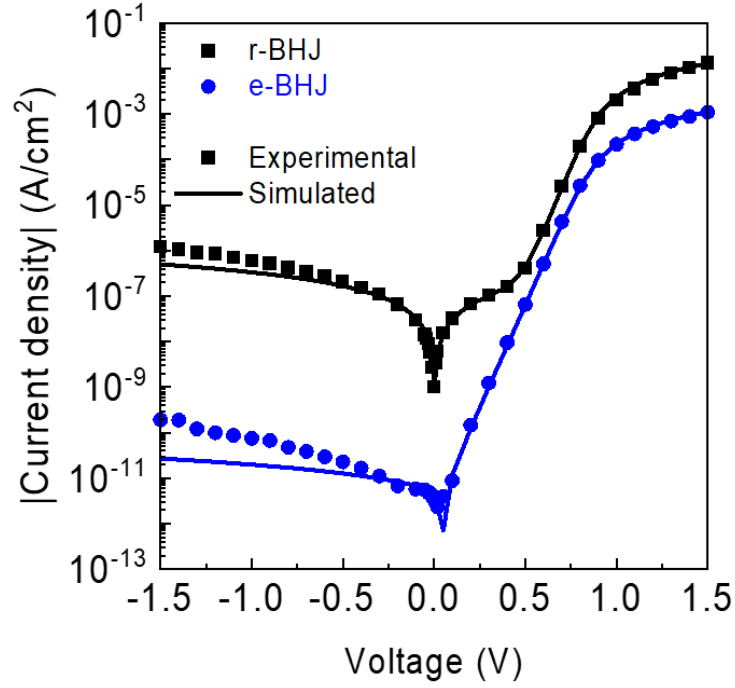


Figure 21 Analysis of dark current density of OPDs. (a) Equivalent circuit model of OPD. (b) Comparison of measured and simulated dark current density of champion OPDs.

As discussed in section 3.4, we use Prince's equivalent circuit model to evaluate the physical parameters such as reverse saturation current density (J_0), diode ideality factor (n), shunt resistance (R_pA), and series resistance (R_sA) where A is the device area.^{46,47} The simulated results for OPDs show high consistency with the experimental data in Figure 21. Upon mixing SEBS in BHJ, R_pA was significantly improved by four orders of magnitude, which leads to a reduction in dark current. However, it is worth noting that J_0 that also has the determining role in reducing dark current remains the same value, 3 pA/cm². R_s was increased by one order of magnitude and n was increased from 1.72 to 1.88 summarized in

Table 1. From equation (22), the high shunt resistance is ideal for minimizing the thermal noise, hence, small dark current values originating from high shunt resistance make them attractive as photodetectors.

Table 1 Physical parameters of OPDs derived from the equivalent circuit model.

OPD Active layer	J_0 (pA/cm²)	n	R_{pA} ($\Omega \cdot \text{cm}^2$)	R_{sA} ($\Omega \cdot \text{cm}^2$)
e-BHJ	3	1.88	7×10^{10}	470
r-BHJ	3	1.72	3×10^6	40

4.2.3 Photodetector Characteristics

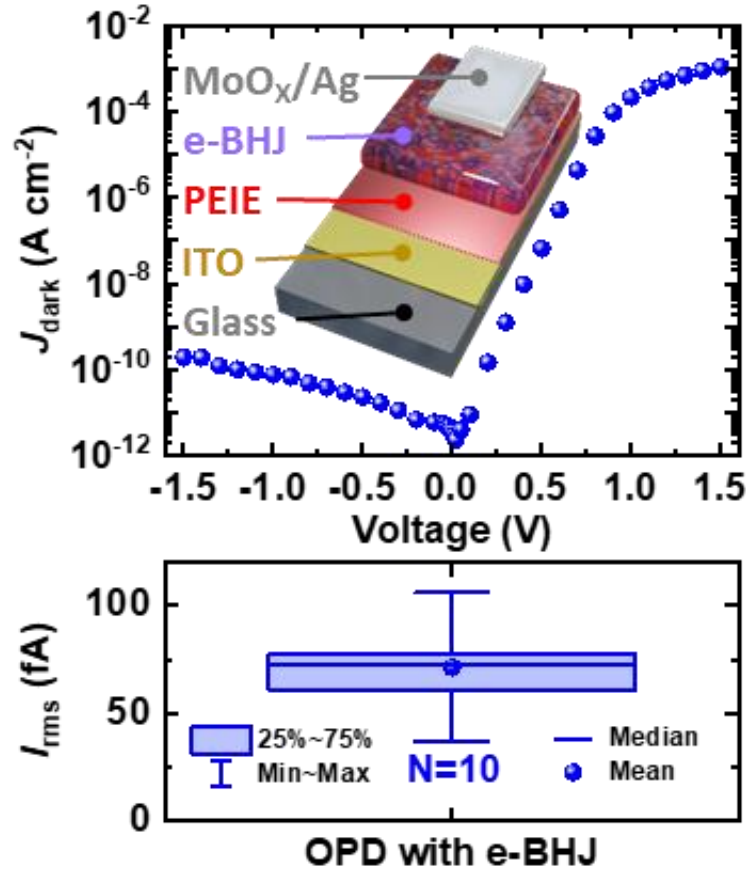


Figure 22 Dark current density (top) and root-mean-squared noise box plot ($N = \#$ of data points) (bottom). The device structure of OPD (inset)

Figure 22 (bottom) shows that the distribution of measured I_{rms} values with a median of 72 fA and at a measurement bandwidth of $B = 1.5$ Hz for different reverse biases in Figure 22 (top). This is comparable to that of low-noise SiPDs (Hamamatsu S1133 series) and state-of-the-art P3HT:ICBA OPDs recently reported.²⁶

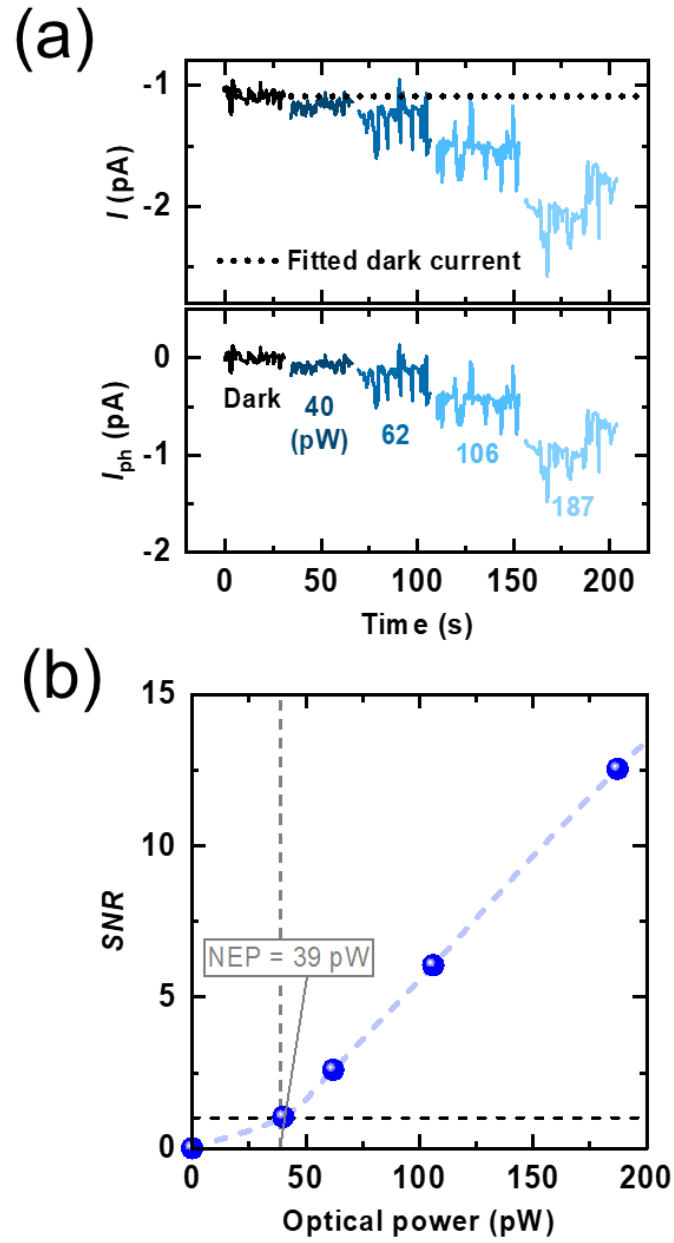


Figure 23 Analysis of photodetector metrics for OPD with e-BHJ on a rigid substrate. (a) Optical power dependence of transient current and photocurrent. (b) Optical power dependence of signal-to-noise ratio.

Figure 23 shows that a direct measurement of the NEP (653 nm, 1.5 Hz) yields a value of 39 pW at 0 V. Note that this value is larger than the value of $NEP_{\text{extrapolated}} = 10$ pW calculated by extrapolating the photocurrent to the median I_{rms} using a $\mathfrak{R}(653 \text{ nm})$ of 7.5 mA/W derived from the photocurrent slope at optical power values between 1 nW and 10 μW (Figure 24). This discrepancy arises because \mathfrak{R} decreases as the optical power approaches the NEP , reaching a value of 1.9 mA/W at the NEP . Similar behavior has been observed in low-noise SiPDs and OPDs, and has been attributed to the presence of traps⁴⁸. Measured NEP values yield a D^* (0.1 cm², 1.5 Hz) of 1.0×10^{10} Jones at 653 nm. Figure 25 (top) shows that, for average optical power values of 27 μW , $\mathfrak{R}(560 \text{ nm})$ reaches a peak value of 71 mA/W which is significantly larger than at the NEP . Assuming that $\mathfrak{R}(653 \text{ nm})$ losses (ca. 75%) at the NEP are similar at other wavelengths, a peak D^* value of 5.3×10^{10} Jones at 560 nm is estimated (Figure 25, bottom).

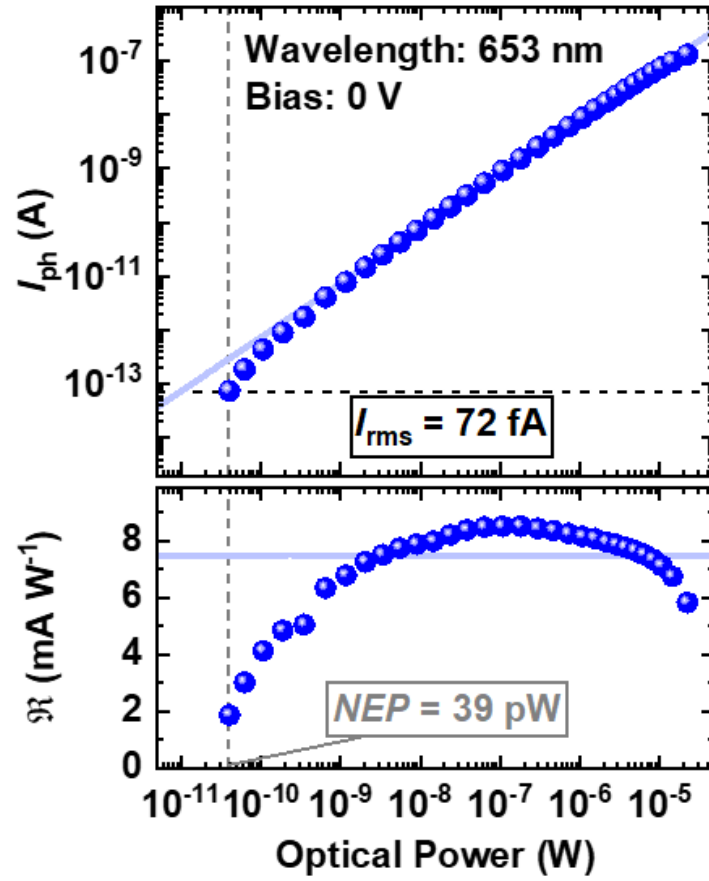


Figure 24 Photocurrent (top) and responsivity (bottom) vs. optical power at a wavelength of 653 nm.

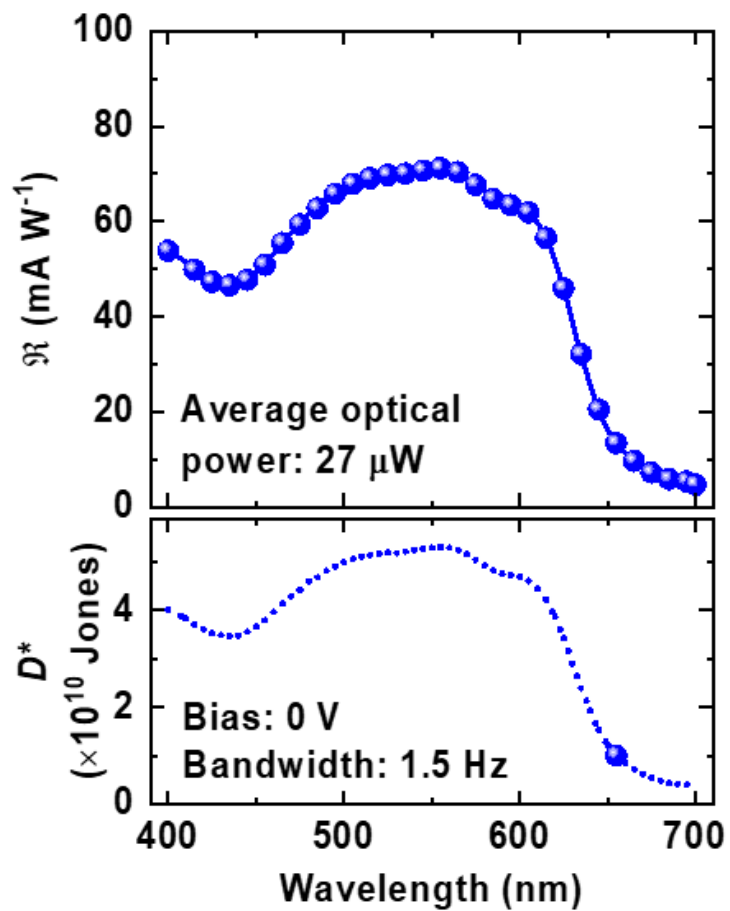


Figure 25 Measured responsivity spectra of OPD with e-BHJ (top). Specific detectivity spectra for the elastomeric OPD normalized at a wavelength of 653 nm using responsivity spectra (bottom).

4.2.4 Response Time

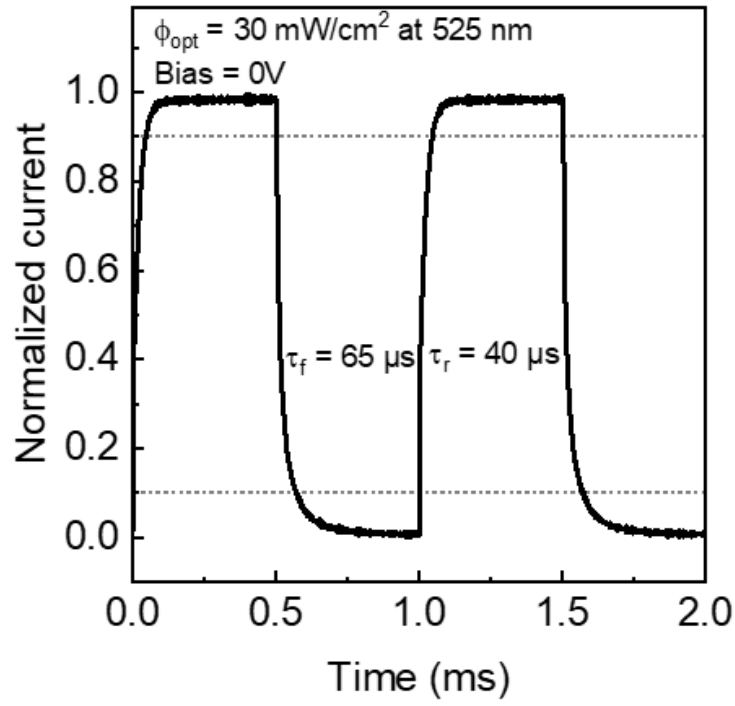


Figure 26 Response time of OPD with e-BHJ.

We investigated the response time of OPD with e-BHJ by connecting it to a transimpedance amplifier circuit with a 3dB bandwidth of 530 kHz and by measuring their response time. As shown in Figure 26, the rise and fall times are 40 μs and 65 μs , respectively, with an irradiance of 30 mW/cm² at 525 nm at the bias of 0 V.

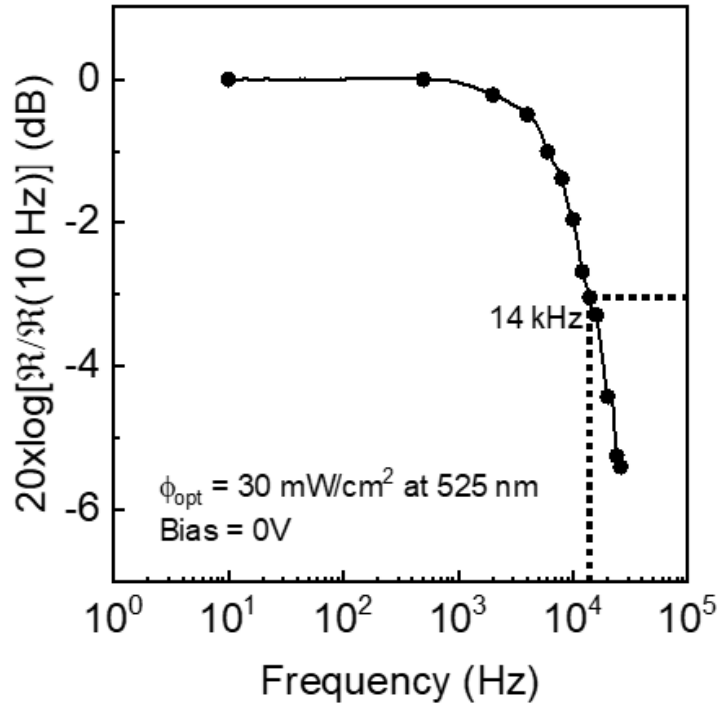


Figure 27 Frequency response of OPD with e-BHJ

Figure 27 shows that a 3 dB normalized responsivity bandwidth for OPD with e-BHJ yields 14 kHz using the same measurement setup as above. As previously discussed,^{26,49} this 3dB bandwidth value is high enough for the applications described in the introduction.

CHAPTER 5. FULLY STRETCHABLE ORGANIC PHOTODIODES (E-OPD)

5.1 Introduction

In this chapter, we will discuss mechanical properties of e-BHJ such as strain at break and Young's modulus (E). Although pristine P3HT:ICBA BHJ layers are not elastomeric, this BHJ has enabled OPDs with a level of performance that is comparable to that of low noise SiPDs.²⁶ Here, we demonstrate stretchable OPDs that using this novel e-BHJ show dark current density values smaller than 600 pA cm^{-2} under reverse bias, but more importantly from a photodetector perspective, a measured median root-mean-squared electronic noise in the tens of femtoampere range and measured NEP values at 653 nm between 13 and 24 pW at strain values up to 60%, yielding D^* values in the 10^{10} Jones range.

5.2 Mechanical characteristics of e-BHJ Film

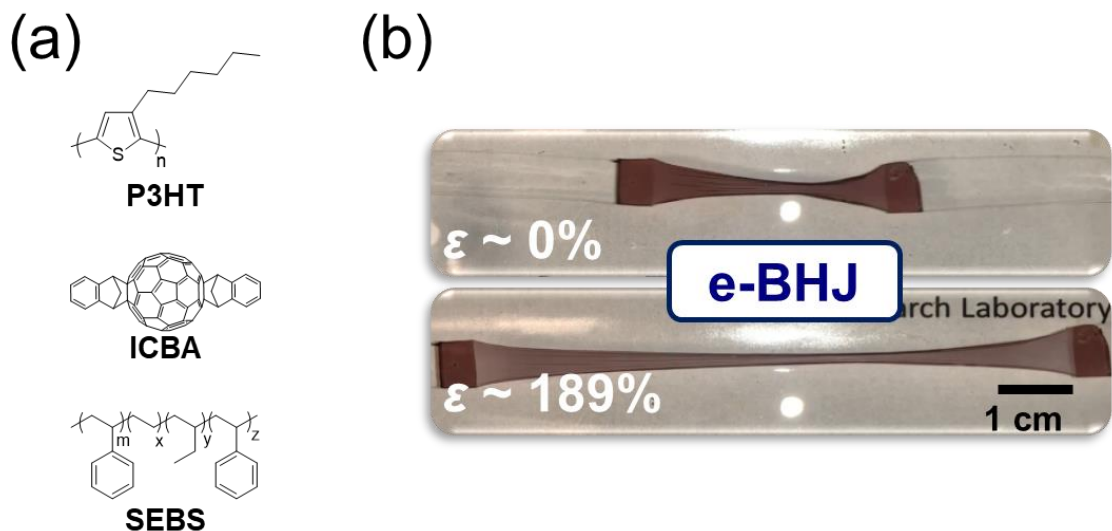


Figure 28 (a) Chemical structure of materials used in r-BHJ and e-BHJ film. (b) A photograph of the relaxed and strained (189 %) e-BHJ film in water.

First, the mechanical properties of freestanding films of e-BHJ were characterized and compared with those of r-BHJ. Figure 28 (a,b) shows the chemical structure of these materials and a photograph of the relaxed and strained e-BHJ in water. Uniaxial tensile tests were performed to plot stress (σ)-strain (ε) curves shown in Figure 29 (a), and the corresponding E and strain at break values were derived in Figure 29 (b). E values are in the range from 259 to 264 MPa for r-BHJ films. The shape of the stress-strain plot derived from these measurements, and consequently E values derived from them, highly depend on stress-strain definitions (e.g. engineering stress-strain, true stress-engineering strain, and true stress-strain) for e-BHJ and SEBS due to the hyperelastic deformation as shown

in Figure 30. Regardless of the definition used, E values are between 2.4 to 6.9 MPa for e-BHJ films and 0.8 to 2.4 MPa for SEBS films; this is, ca. two orders of magnitude smaller than in r-BHJ. Additionally, the strain at break increases from 6% in r-BHJ films to 189% in e-BHJ films; similar to values measured in pristine SEBS films in Table 2 and comparable to those of human tissues.³⁰

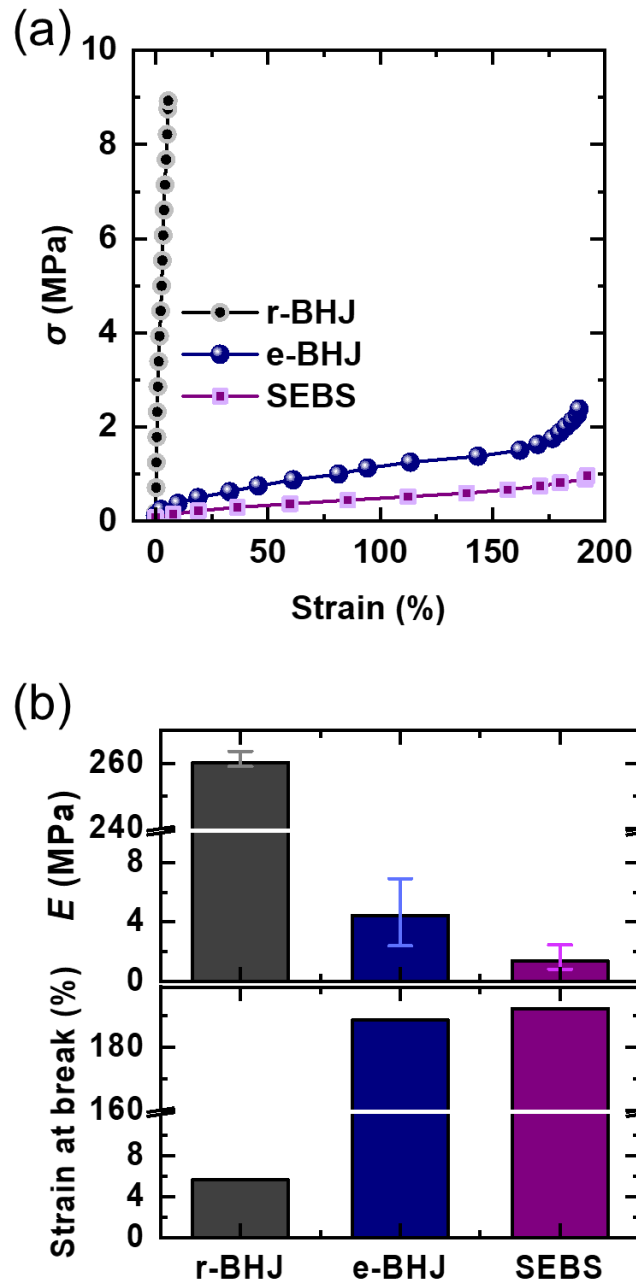


Figure 29 (a) Stress (σ) vs. strain (ϵ) behavior of r-BHJ, e-BHJ, and SEBS from the uniaxial tensile test. (b) Range of Young's moduli (E) using different stress-strain definitions. The error bars represent the minimum and maximum bounds of E (top). Strain at break compared to the initial length (bottom).

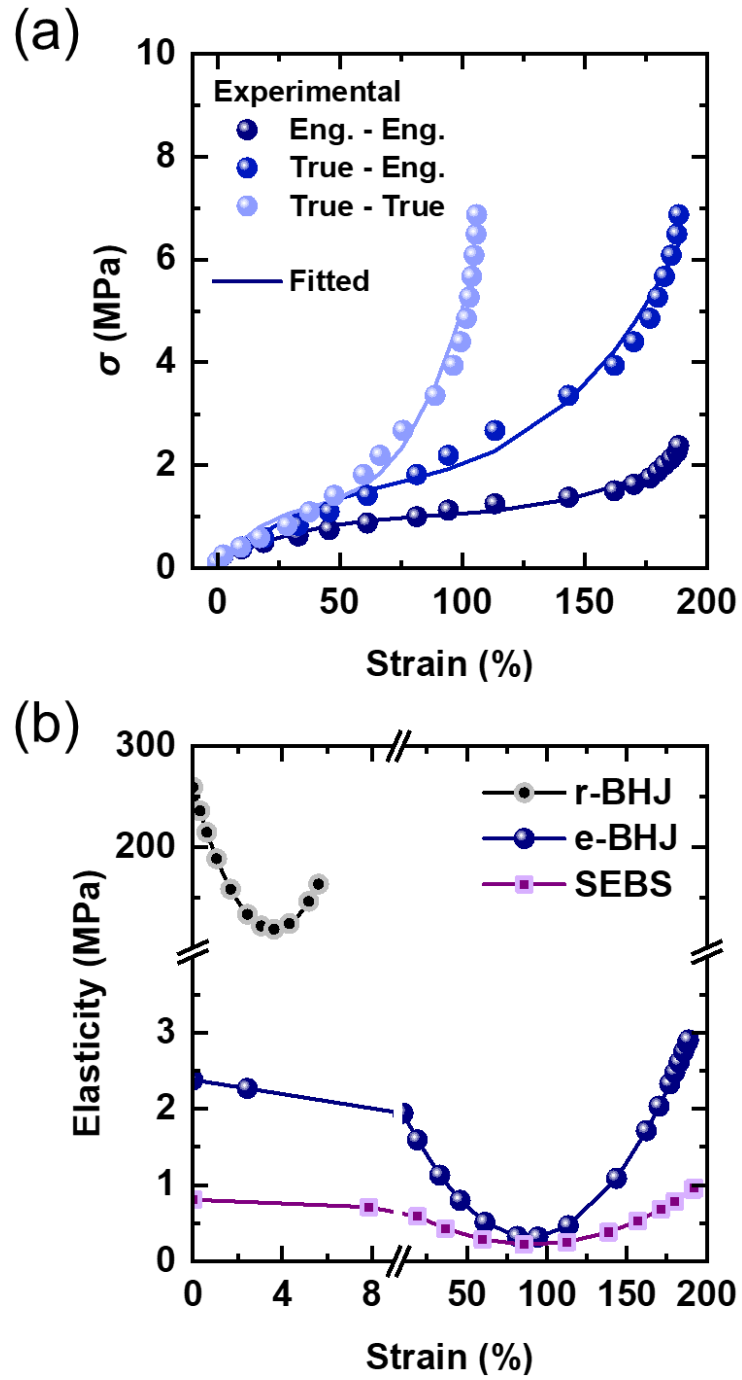


Figure 30 (a) Comparison of experimental and fitted stress curve of e-BHJ. (b) Elasticity vs. strain plot derived from the engineering stress-strain curve.

Figure 30 (a) illustrates a comparison of the stress-strain curve between engineering stress-strain (Eng. - Eng.), true stress-engineering strain (True - Eng.), and true stress-strain (True - True) on the mechanical behavior of e-BHJ. The nonlinear stress-strain curves were fitted to a third-order polynomial equation, and the elasticity was calculated via the derivative of the third-order polynomial equation in Figure 30 (b).

Table 2 Mechanical properties of freestanding films extracted from the stress-strain plots.

Film	Tensile Modulus (MPa)	Modulus of Toughness (MJ/m³)	Strain at Break (%)	Tensile Strength (MPa)
e-BHJ	2.4	2.2	189	2.4
r-BHJ	259	0.3	6	9.3
Pristine SEBS	0.8	1.0	192	0.9

5.3 Stretchable Electrodes

Unlike FETs, since the area where charges are generated for OPDs is directly overlapped with the electrodes, therefore, a small crack on the photoactive layer under strains results in short-circuited and critical failure. Several groups have demonstrated stretchable electrodes using carbon nanotubes,⁵⁰ silver nanowires,³³ and Graphene.⁵¹ However, these nanomaterials have inherently high surface roughness and low conductivity compared to conventional metals. An alternative solution, though with

slightly more complicated is to use a conducting polymer, PEDOT:PSS which possesses excellent mechanical flexibility, high optical transparency, and facile solution processability. In an attempt to impart stretchability on PEDOT:PSS, the introduction of ionic liquid or plasticizer into PEDOT:PSS to provide a free volume is not yet reliable.^{44,45} In reality, since OPDs using pre-strained PEDOT:PSS as bottom electrode has long been demonstrated,^{13,14} a practical alternative is to use PEDOT:PSS on strained PDMS.

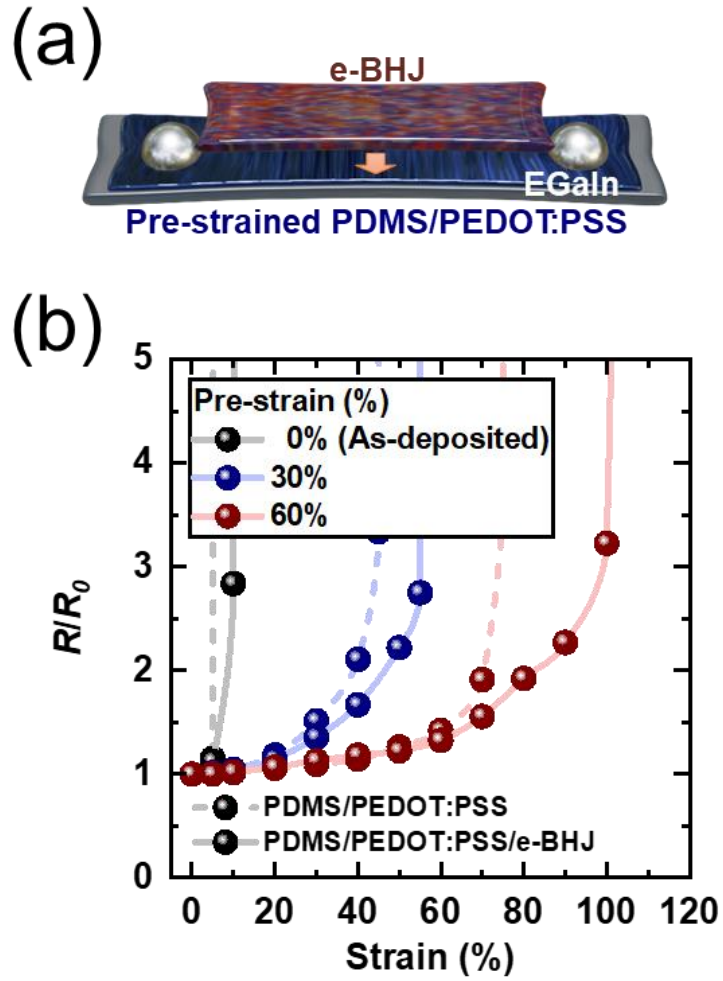


Figure 31 (a) Structure of pre-strained PDMS/PEDOT:PSS electrode. (b) Normalized resistance vs. strain plot.

Figure 31 (a) shows the structure of pre-strained PDMS/PEDOT:PSS electrode. The fabrication details are discussed in section 3.2.3. As shown in Figure 31 (b), Even though the PDMS/PEDOT:PSS without pre-strain electrically and mechanically failed at a strain value of 5%, the normalized resistance of 30% pre-strained PDMS/PEDOT:PSS is electrically functional up to 60% strain value. Moreover, it was found that 60% pre-strained PDMS/PEDOT:PSS film sustains significantly larger strain values. This data supports that strain at failure is highly dependent on the amount of pre-strain of PDMS.

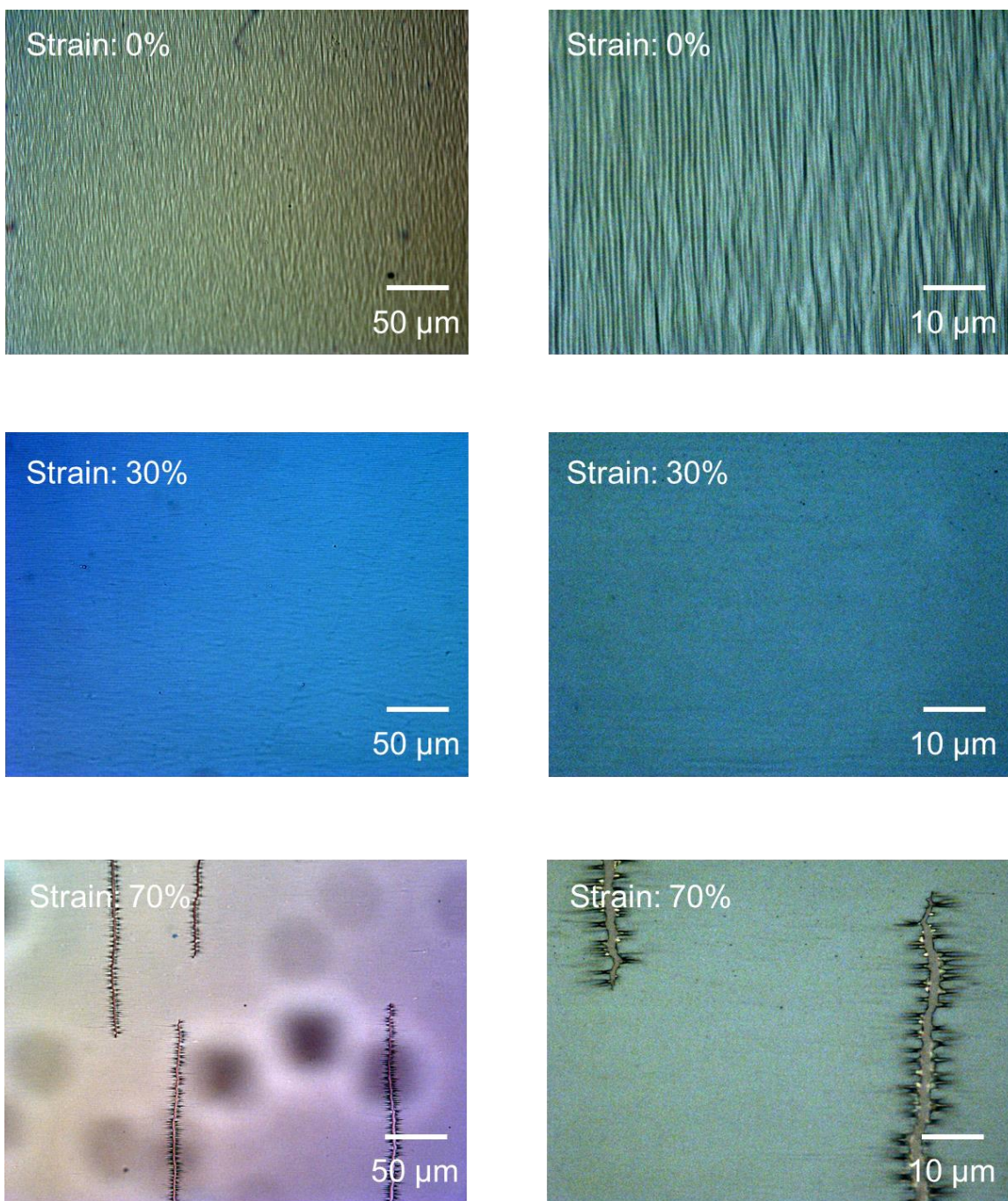


Figure 32 Optical microscopy image for 30% pre-strained PDMS/PEDOT:PSS under different strains

Figure 32 shows the optical microscopy image for 30% pre-strained PDMS/PEDOT:PSS under different strains. Under strain value of 0%, PEDOT:PSS is wrinkled due to lateral compression stress. As increases in the strain to 30% used during PEDOT:PSS deposition, the wrinkles disappear. However, it was found that cracks start to be generated under a strain of 70%. This is consistent with the failure of pre-strained PDMS/PEDOT:PSS occurs in the vicinity of 60% shown in Figure 31 (b). To further enhance the stretchability of the electrode, PEDOT:PSS was spin-coated on a 60% pre-strained PDMS film, shown in Figure 33. There is no sign of cracks until a strain of 160%. These results show that applying more pre-strain on PDMS improves the stretchability of the electrode. However, once released from strain of PDMS upon deposition of PEDOT:PSS, lateral cracks are generated due to the vertical tensile stress on the films based on Poisson effect. This could potentially lead to being short-circuited when combining with e-BHJ on top of the electrode. Practically, 30% pre-strain PDMS/PEDOT:PSS is a better option for fully stretchable OPD.

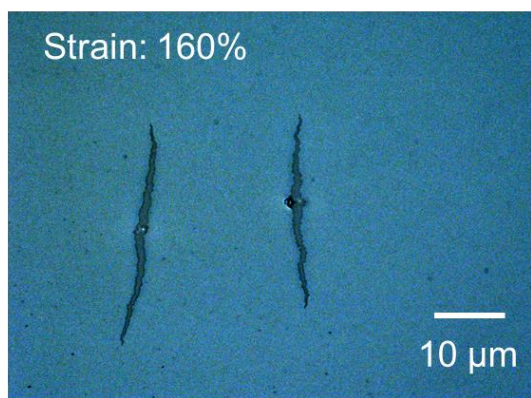
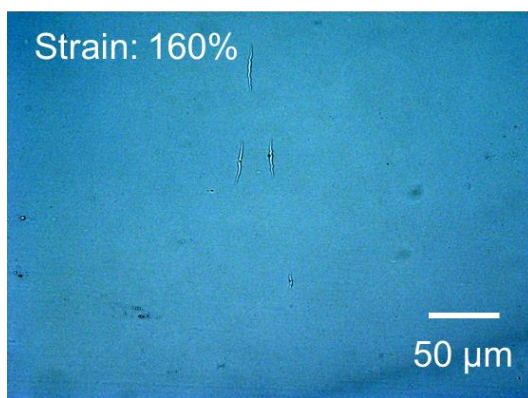
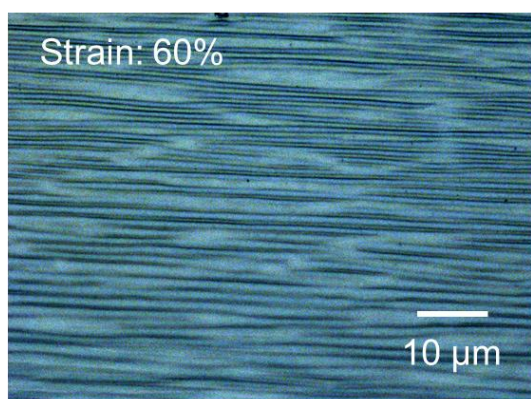
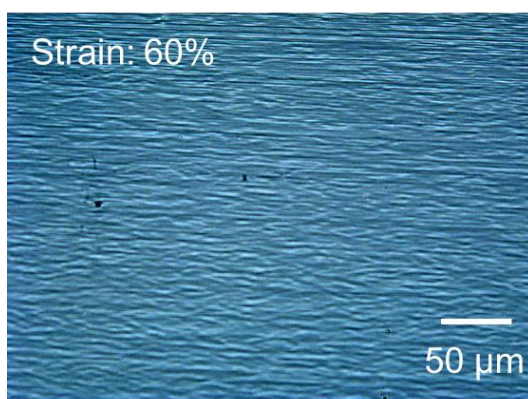
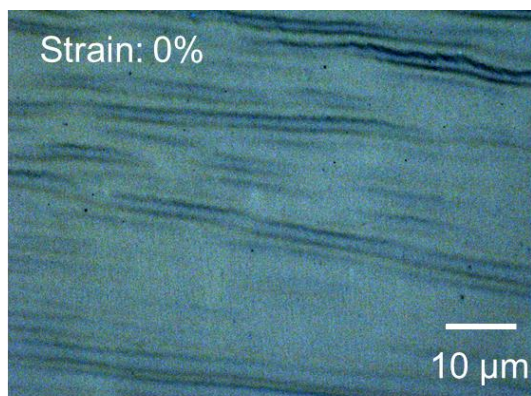
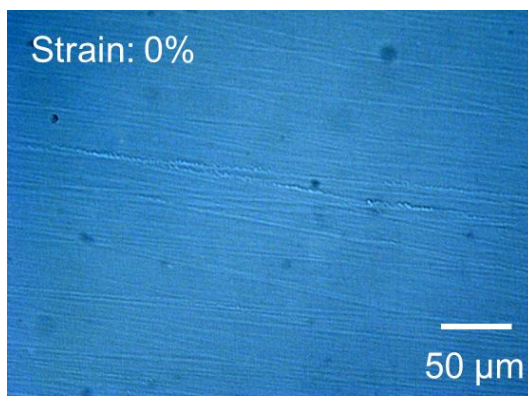


Figure 33 Optical microscopy image for 60% pre-strained PDMS/PEDOT:PSS under different strains

5.4 Optoelectrical characteristics of e-OPDs

5.4.1 Photodetector characteristics

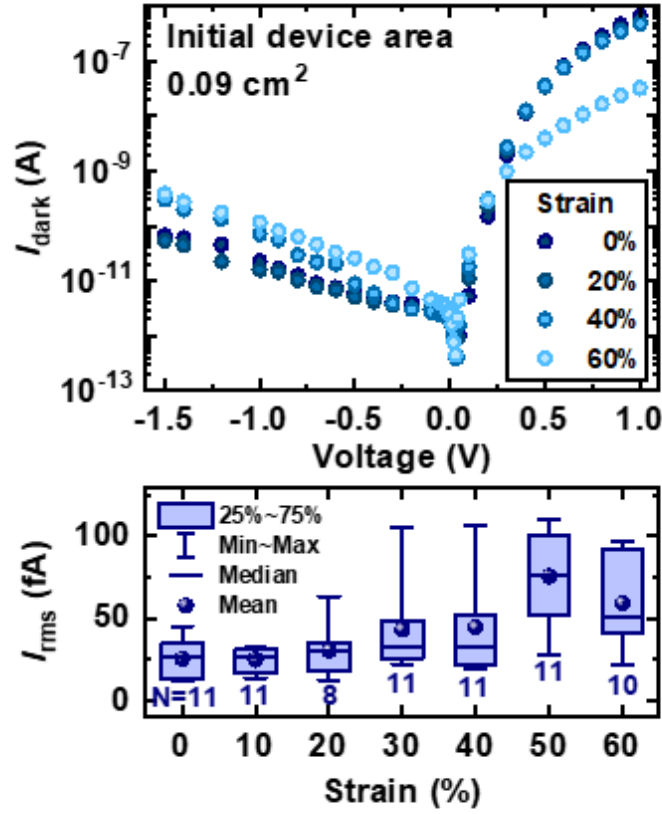


Figure 34 Dark current (top) and root-mean-squared noise box plot (bottom) under different strains.

We now demonstrate the use of e-BHJ films to realize elastomeric OPDs, hereon referred to as e-OPD. The fabrication process and structure of e-OPD with an e-BHJ was discussed in section 3.2.3. A key difference with respect to previous work is that, in the

first step, only PEDOT:PSS was spin-coated directly onto a 30% pre-strained PDMS film. In the second step, the substrate was released and the e-BHJ was spin-coated on top of the buckled PDMS/PEDOT:PSS substrate. In such geometry, the e-BHJ experiences not only flexural deformation but also elastic deformation. Last, a drop of eutectic metal GaIn was used as top electrode. The photodetector characteristics of e-OPDs were then measured as a function of strain. Note that the e-OPD was released to 0% strain between different strain values. Figure 34 (top) shows that I_{dark} vs. V characteristics of e-OPDs are comparable to those measured on OPDs with an e-BHJ on rigid glass substrates and remain comparable under reverse bias up to 60% strain.

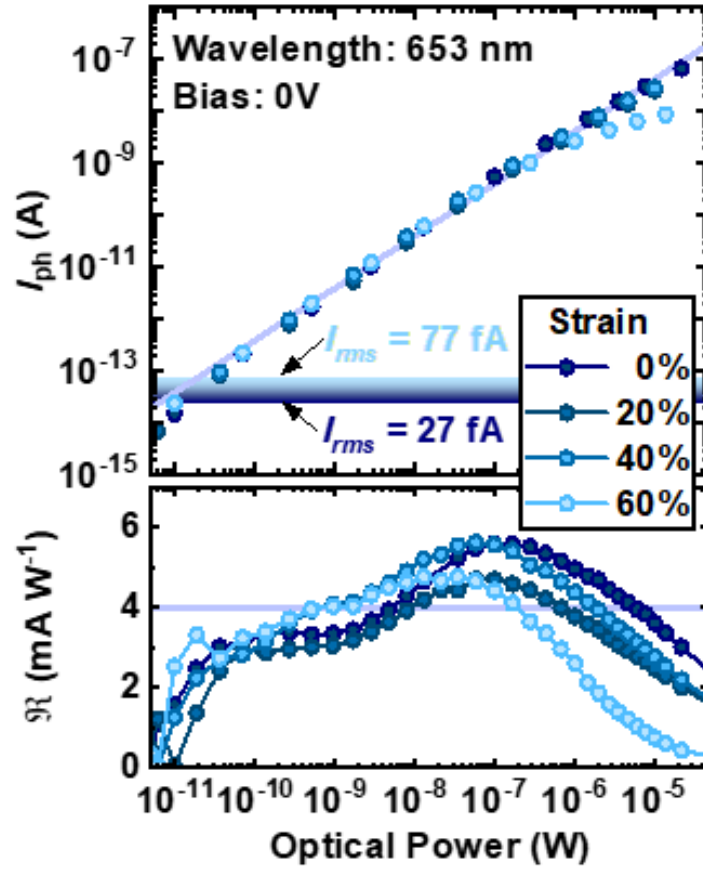


Figure 35 Optical power-dependent photocurrent (top) and responsivity (bottom) under different strains

Furthermore, Figure 34 (bottom) shows that the distribution of I_{rms} values is similar to those found on OPDs with e-BHJ on a rigid substrate, with median values of 27 fA in unstrained e-OPD and 51 fA at 60% strain. Figure 35 shows that up to a strain value of 60%, the photocurrent varies approximately linearly with optical power for values between 1 nW and 1 μ W, yielding a $\mathfrak{R}(653 \text{ nm})$ of 4 mA/W. Deviations at optical power values larger than 1 μ W are caused by the increased series resistance when e-OPDs are subjected to 60% strain (Figure 34, top). At values below 100 pW, $\mathfrak{R}(653 \text{ nm})$ decreases as the optical power approaches the *NEP*.

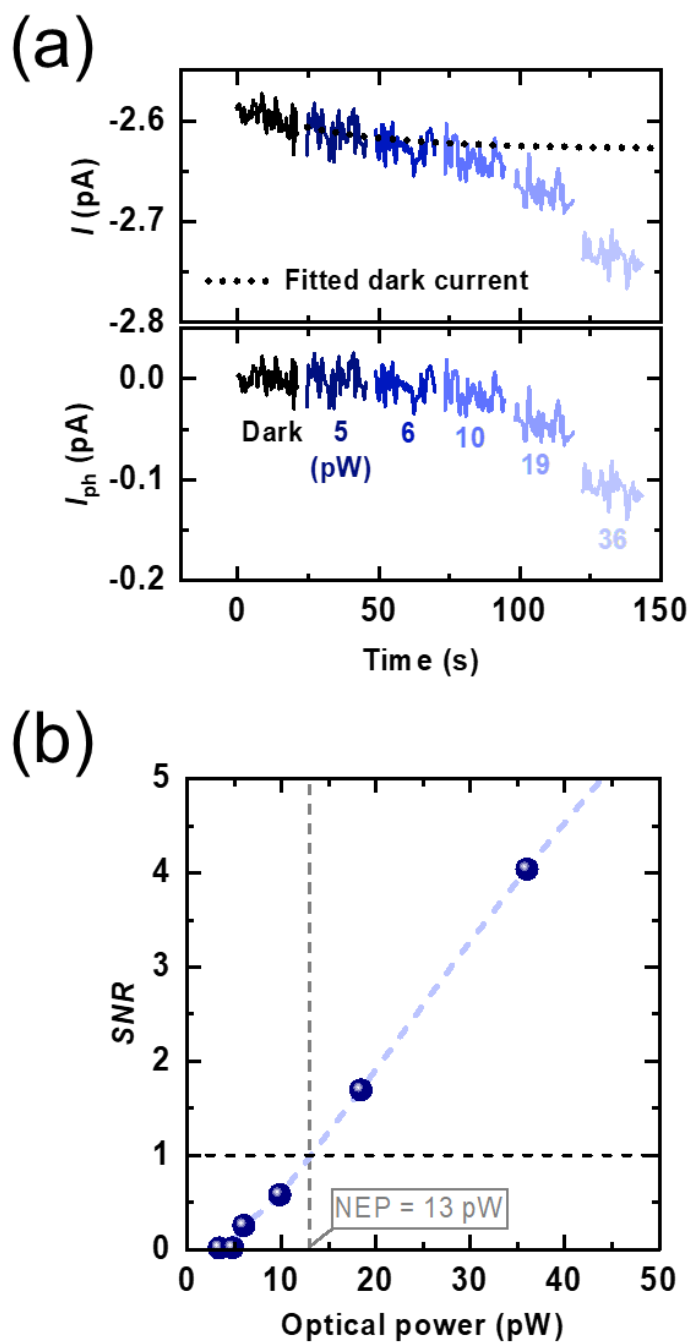


Figure 36 Analysis of photodetector metrics for unstrained e-OPD. (a) Optical power dependence of transient current and photocurrent. (b) Optical power dependence of signal-to-noise ratio.

Figure 36 shows that unstrained e-OPDs yield a NEP value of 13 pW. Figure 37 (top) shows that NEP values (653 nm, 1.5 Hz) at 0 V are in the range between 13 and 24 pW for e-OPDs strained up to 60%. These values are consistent with values measured on rigid OPDs with an e-BHJ and demonstrate that e-OPDs can sustain up to 60% strain without substantial degradation, yielding an average D^* value of 2.3×10^{10} Jones (Figure 37, bottom) at 653 nm.

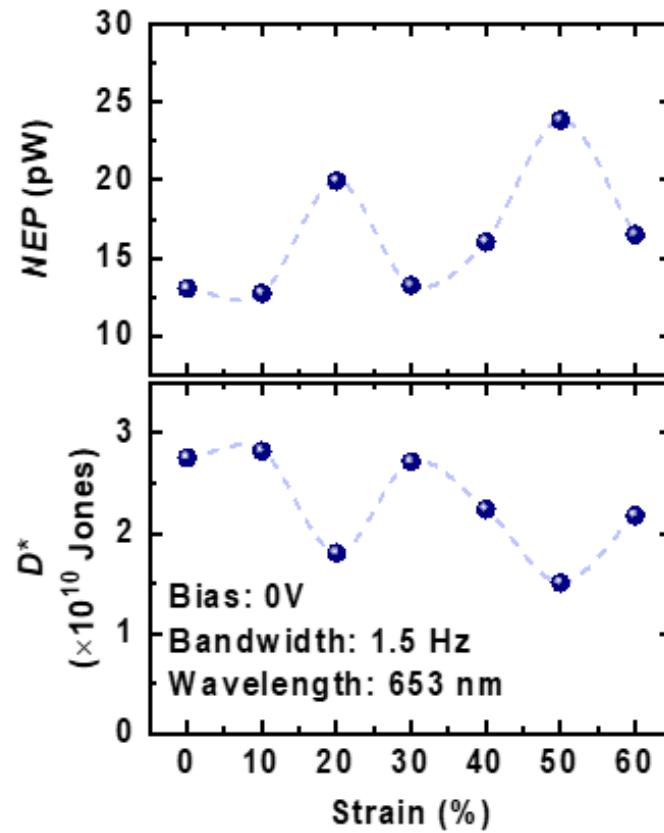


Figure 37 Noise equivalent power (top) and specific detectivity (bottom) under different strains

Beyond strain values of 60%, the e-OPDs failed. As discussed in Figure 31 (b) this is because the normalized resistance (R/R_0) of as-deposited and pre-strained PDMS/PEDOT:PSS increases rapidly when the applied strain surpasses the PDMS strain used during PEDOT:PSS deposition. However, it was found that pre-strained PDMS/PEDOT:PSS/e-BHJ films can sustain significantly larger strain values. This data supports that failure of e-OPDs beyond 60% strain is caused by failure of the 30% pre-strained PDMS/PEDOT:PSS electrode rather than the e-BHJ layer. To further confirm this, e-OPDs were fabricated on 60% pre-strained PDMS/PEDOT:PSS electrodes. Figure 38 (top) shows that the I_{dark} vs. V characteristics of e-OPDs are even superior to those found on e-OPDs shown in Figure 34 (top) as they sustain strain values up to 100% without substantial degradation. Furthermore, the distribution of I_{rms} values shown in Figure 38 (bottom) remains similar to those found on rigid OPDs with an e-BHJ and e-OPDs shown in Figure 34 (bottom), with median values between 30 and 38 fA for strain values up to 100%.

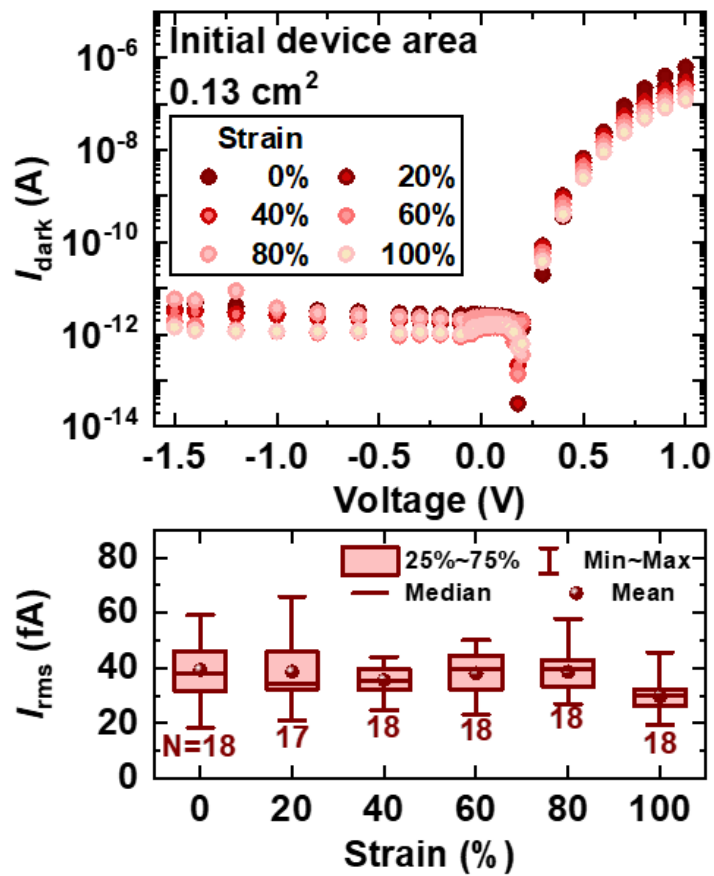


Figure 38 Dark current (top) and root-mean-squared noise box plot (bottom) of e-OPD using 60% pre-strained PDMS/PEDOT:PSS.

5.4.2 Response Time

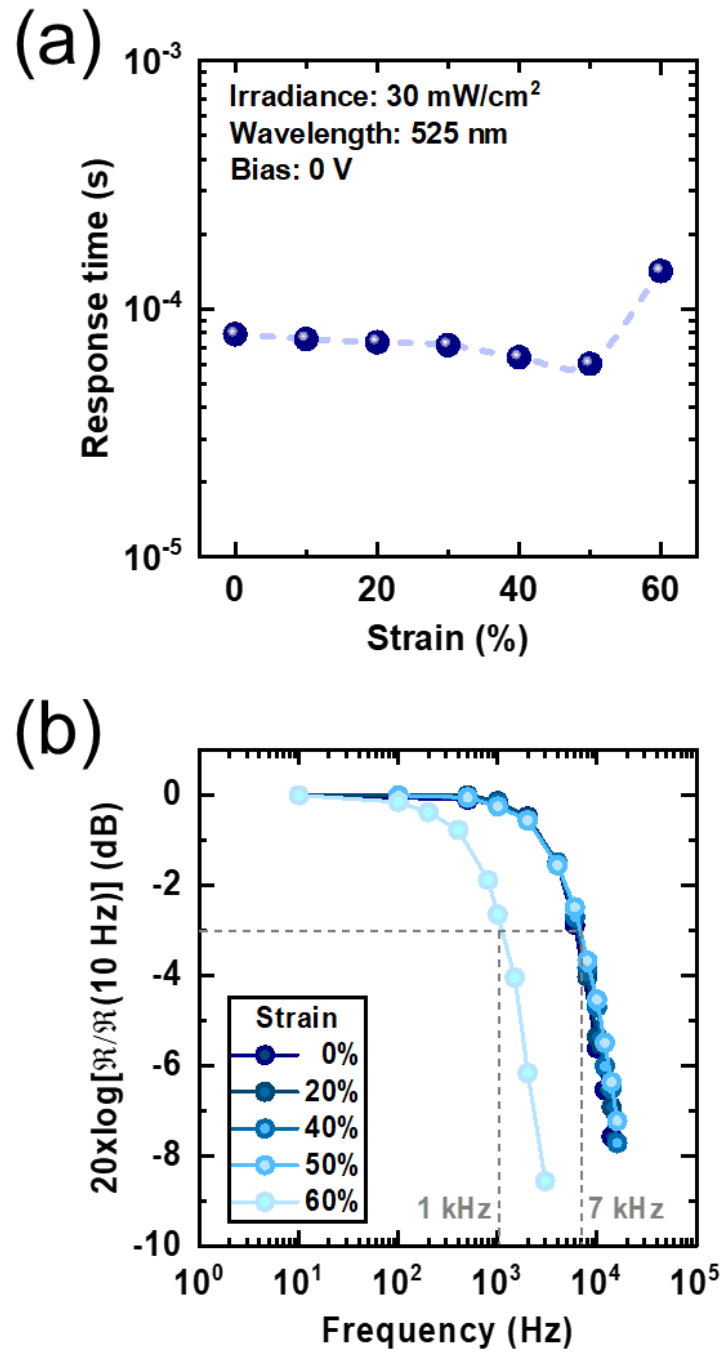


Figure 39 Response time of e-OPD under different strains. (a) 10%-90% response time. (b) Frequency-dependent normalized responsivity.

We investigated the response time of e-OPD by connecting them to a transimpedance amplifier circuit with a 3 dB bandwidth of 530 kHz and by measuring their response time. As shown in Figure 39 (a), response time values ranged from 60 μ s to 79 μ s up to 50% of strain, then doubled to 142 μ s at 60% strain. This increase is correlated with an RC time increase due to the increased resistance of pre-strained PDMS/PEDOT:PSS, as shown in Figure 31 (b). Figure 39 (b) shows that a 3dB normalized responsivity bandwidth of 7 kHz is maintained up to ca. 50% of strain and falls to 1 kHz at 60% strain. Similar to rigid OPD, these 3dB bandwidth values are sufficiently high for the range of applications such as PPG sensors.

5.5 Operational Stability in Ambient Air

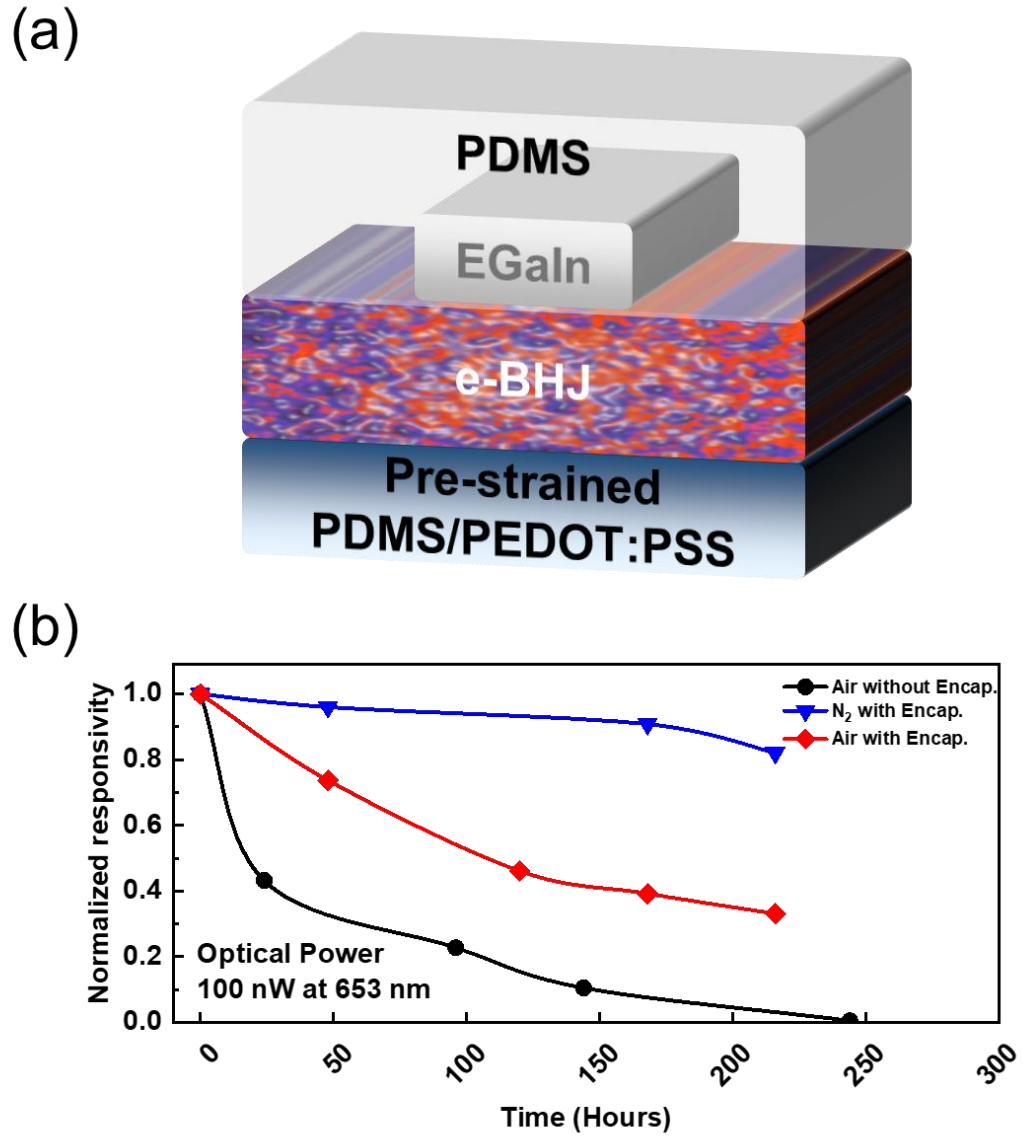


Figure 40 (a) Structure of e-OPD with encapsulation (b) Normalized responsivity vs. Exposure time under different conditions

In an attempt to investigate operational stability in ambient air, As shown in Figure 40 (a), the PDMS was poured on top of e-OPD. Then the sample was stored for 72 hours at room temperature in an N₂-filled glove box to solidify PDMS. Figure 40 shows the normalized responsivity under different conditions. The device without encapsulation exhibits complete failure after 244 hours in an ambient atmosphere. However, the device with encapsulation maintains 30% of the original responsivity. Although the device with encapsulation in an ambient atmosphere was degraded severely compared with the device in an N₂-filled atmosphere, it was found that PDMS encapsulation delays the photooxidation reactions of donors and acceptors. ⁵²⁻⁵⁴

CHAPTER 6. CONCLUSION AND FUTURE WORK

6.1 Conclusion

This dissertation reports on the first demonstration of stretchable organic photodiodes using an elastomeric organic photoactive layer comprising a blend of the soft elastomer matrix SEBS, with the donor polymer P3HT, and the acceptor ICBA. Bulk heterojunctions constitute the basis of organic photodiodes used for either photovoltaic or photodetector applications. This elastomeric bulk heterojunction photoactive layer shows skin-like mechanical properties, i.e. Young's modulus values in the range from 2.4 to 6.9 MPa and strain at break of 189%. Most bulk heterojunctions in the literature cannot be considered as elastomeric bulk heterojunction because they have larger Young's modulus values in the range from 200 MPa to 1 GPa, which are two orders of magnitude larger than values of human tissues (< 30 MPa) and typical elastomers (e.g. PDMS and SEBS). In addition to skin-like mechanical properties, these elastomeric bulk heterojunctions yield elastomeric organic photodiodes using pre-strained PDMS/PEDOT:PSS with measured electronic noise currents ranging from 27 fA to 51 fA and NEP values from 13 pW to 24 pW at a wavelength of 653 nm with a bias of 0 V when subjected to strain values of up to 60%. Especially, the photocurrent varies approximately linearly with optical power, yielding a responsivity of 4 mA/W and the average specific detectivity of 2.3×10^{10} Jones at a wavelength of 653 nm with a bias of 0 V, which is two orders of magnitude lower than that of rigid commercially available low-noise SiPDs and state-of-the-art P3HT:ICBA organic photodiodes. Furthermore, the response times of elastomeric organic photodiodes

are maintained in the range of 60 μ s to 79 μ s up to 50% of strain, then doubled to 142 μ s at 60% strain. This yields a 3 dB normalized responsivity bandwidth of 7 kHz up to 50% of strain, which is sufficiently high for the range of biomedical applications such as PPG sensors. Although examples of stretchable organic photodiodes in the context of photodetection exist in the literature, they use non-elastomeric bulk heterojunction laminated onto a pre-strained substrate and their performance metrics were not measured beyond their dark current density, which is approximately 2 orders of magnitude larger than the one measured in our photodiodes. Hence, the stretchable organic photodiodes using an elastomeric organic photoactive layer reported in this work do not only show skin-like mechanical properties but they also define the state-of-the art in terms of performance with an improvement of two orders of magnitude in dark current density compared to prior art. Therefore, the detailed characterization and measured level of performance of our elastomeric organic photodiodes should be considered a new milestone in the field of stretchable photodetectors.

This research is expected to be of great help in breaking the boundary between the biological world and digital devices by providing a proof-of-principle demonstration that the approach to engineer intrinsically stretchable photoactive layers helps organic photodiodes maintain their mechanical and optoelectrical performance up to 60% of tensile strain. This unique combination of properties could enable a myriad of new applications such as a skin-mounted sensor that can measure body signals at any time, sensors for artificial eyes, and artificial skin for soft robots by enabling the seamless integration of optoelectronics with soft materials.

6.2 Future Work

6.2.1 *Monitoring Photoplethysmogram (PPG)*

PPG is a noninvasive technique that optically detects the changes of blood vessel volume in the microvascular bed of tissues for heart rate monitoring. The volume of subdermal blood vessels changes as the arterial pulsation, which in turn leads to the absorptive, reflective, and scattered light through the skin. Thus, the photodetector can monitor the pulsation signals, including diastolic and systolic signals. For this reason, to accurately detect the bio-signal, the adhesion between the skin and the photodetector is critical. The stretchable photodetector we developed has Young's modulus similar to that of skin and has high detectivity so that PPG signal can be monitored sufficiently. Since it was confirmed that our device with encapsulation works well in an ambient atmosphere, the measurement of body signal with e-OPD will be the subject of future work.

6.2.2 *Phosphomolybdic Acid (PMA) Doping*

A drawback of the device we developed above is the use of liquid metal. Since all layers except for EGaIn are made of thin films spin-coated, the whole structure of the device inherently has instability due to the liquid properties of EGaIn. To overcome this, a thin hole collecting layer can be created by doping PMA on top of e-BHJ to replace liquid metal. In addition, This can replace opaque EGaIn, making all layers semi-transparent as

well as stretchable. It can be potentially used for windows in buildings or where transparency is required.

6.2.3 *Stretchable OPV Device*

A highly stretchable organic photovoltaic device applies to solar roofing on non-planar surfaces of vehicles and buildings, and powering system on robotic limbs for conformable coverage.⁵⁵ However, the existing donor and acceptor materials for OPV applications do not possess elastomeric properties. Recently, the emergence of non-fullerene acceptors enabled single-junction OPVs to achieve PCE as high as 15.6% using PBDB-TF as a donor.⁵⁶ Since SEBS is well miscible in most organic solvents, our preliminary results potentially show that blending elastomeric SEBS into a high-efficiency donor such as PBDB-TF or PTB7 and non-fullerene acceptor, such as ITIC derivatives or Y6, which can cover Vis-NIR range, may open a new way of universally imparting stretchability on organic BHJ film.

REFERENCES

- 1 Khan, Y., Ostfeld, A. E., Lochner, C. M., Pierre, A. & Arias, A. C. Monitoring of Vital Signs with Flexible and Wearable Medical Devices. *Advanced Materials* **28**, 4373-4395, doi:10.1002/adma.201504366 (2016).
- 2 Park, S. *et al.* Ultraflexible Near-Infrared Organic Photodetectors for Conformal Photoplethysmogram Sensors. *Advanced Materials* **30**, 1802359, doi:10.1002/adma.201802359 (2018).
- 3 Yokota, T. *et al.* Ultraflexible organic photonic skin. *Science Advances* **2**, e1501856, doi:10.1126/sciadv.1501856 (2016).
- 4 Gogurla, N., Roy, B., Min, K., Park, J. Y. & Kim, S. A Skin-Inspired, Interactive, and Flexible Optoelectronic Device with Hydrated Melanin Nanoparticles in a Protein Hydrogel–Elastomer Hybrid. *Advanced Materials Technologies* **5**, 1900936, doi:10.1002/admt.201900936 (2020).
- 5 Lee, Y. *et al.* Stretchable organic optoelectronic sensorimotor synapse. *Science Advances* **4**, eaat7387, doi:10.1126/sciadv.aat7387 (2018).
- 6 Kim, R.-H. *et al.* Waterproof AlInGaP optoelectronics on stretchable substrates with applications in biomedicine and robotics. *Nature Materials* **9**, 929-937, doi:10.1038/nmat2879 (2010).
- 7 Lee, H. *et al.* Stretchable organic optoelectronic devices: Design of materials, structures, and applications. *Materials Science and Engineering: R: Reports* **146**, 100631, doi:10.1016/j.mser.2021.100631 (2021).
- 8 Ko, H. C. *et al.* A hemispherical electronic eye camera based on compressible silicon optoelectronics. *Nature* **454**, 748, doi:10.1038/nature07113 (2008).
- 9 Zhang, D. *et al.* OptoSense. *Proceedings of the ACM on Interactive, Mobile, Wearable and Ubiquitous Technologies* **4**, 1-27, doi:10.1145/3411826 (2020).
- 10 Lacour, S. P., Jones, J., Wagner, S., Teng, L. & Zhigang, S. Stretchable Interconnects for Elastic Electronic Surfaces. *Proceedings of the IEEE* **93**, 1459-1467, doi:10.1109/JPROC.2005.851502 (2005).
- 11 Axisa, F. *et al.* in *Polytronic 2007 - 6th International Conference on Polymers and Adhesives in Microelectronics and Photonics*. 280-286.
- 12 Song, Y. M. *et al.* Digital cameras with designs inspired by the arthropod eye. *Nature* **497**, 95-99, doi:10.1038/nature12083 (2013).

- 13 Lipomi, D. J., Tee, B. C. K., Vosgueritchian, M. & Bao, Z. Stretchable Organic Solar Cells. *Advanced Materials* **23**, 1771-1775, doi:10.1002/adma.201004426 (2011).
- 14 Kaltenbrunner, M. *et al.* Ultrathin and lightweight organic solar cells with high flexibility. *Nature Communications* **3**, doi:10.1038/ncomms1772 (2012).
- 15 Jinno, H. *et al.* Stretchable and waterproof elastomer-coated organic photovoltaics for washable electronic textile applications. *Nature Energy* **2**, 780-785, doi:10.1038/s41560-017-0001-3 (2017).
- 16 Trung, T. Q. & Lee, N.-E. Recent Progress on Stretchable Electronic Devices with Intrinsically Stretchable Components. *Advanced Materials* **29**, 1603167, doi:10.1002/adma.201603167 (2017).
- 17 Bauer, S. *et al.* 25th anniversary article: A soft future: from robots and sensor skin to energy harvesters. *Adv Mater* **26**, 149-161, doi:10.1002/adma.201303349 (2014).
- 18 Han, C.-W. *et al.* Advanced technologies for UHD curved OLED TV. *Journal of the Society for Information Display* **22**, 552-563, doi:10.1002/jsid.287 (2014).
- 19 Roth, B. *et al.* Mechanical Properties of a Library of Low-Band-Gap Polymers. *Chemistry of Materials* **28**, 2363-2373, doi:10.1021/acs.chemmater.6b00525 (2016).
- 20 Oh, J. Y. *et al.* Intrinsically stretchable and healable semiconducting polymer for organic transistors. *Nature* **539**, 411-415, doi:10.1038/nature20102 (2016).
- 21 Savagatrup, S., Makaram, A. S., Burke, D. J. & Lipomi, D. J. Mechanical Properties of Conjugated Polymers and Polymer-Fullerene Composites as a Function of Molecular Structure. *Advanced Functional Materials* **24**, 1169-1181, doi:10.1002/adfm.201302646 (2014).
- 22 Xu, J. *et al.* Highly stretchable polymer semiconductor films through the nanoconfinement effect. *Science* **355**, 59-64, doi:10.1126/science.aah4496 (2017).
- 23 Sariciftci, N. S. *et al.* Semiconducting polymer-buckminsterfullerene heterojunctions: Diodes, photodiodes, and photovoltaic cells. *Applied Physics Letters* **62**, 585-587, doi:10.1063/1.108863 (1993).
- 24 Yu, G., Gao, J., Hummelen, J. C., Wudl, F. & Heeger, A. J. Polymer Photovoltaic Cells: Enhanced Efficiencies via a Network of Internal Donor-Acceptor Heterojunctions. *Science* **270**, 1789-1791, doi:10.1126/science.270.5243.1789 (1995).
- 25 Yu, G., Pakbaz, K. & Heeger, A. J. Semiconducting polymer diodes: Large size, low cost photodetectors with excellent visible-ultraviolet sensitivity. *Applied Physics Letters* **64**, 3422-3424, doi:10.1063/1.111260 (1994).

- 26 Fuentes-Hernandez, C. *et al.* Large-area low-noise flexible organic photodiodes for detecting faint visible light. *Science* **370**, 698-701, doi:10.1126/science.aba2624 (2020).
- 27 Savagatrup, S. *et al.* [70]PCBM and Incompletely Separated Grades of Methanofullerenes Produce Bulk Heterojunctions with Increased Robustness for Ultra-Flexible and Stretchable Electronics. **27**, 3902-3911, doi:10.1021/acs.chemmater.5b00638 (2015).
- 28 Qin, J. *et al.* Recent Progress in Flexible and Stretchable Organic Solar Cells. *Advanced Functional Materials* **30**, 2002529, doi:10.1002/adfm.202002529 (2020).
- 29 Kendall, M. A. F., Chong, Y.-F. & Cock, A. The mechanical properties of the skin epidermis in relation to targeted gene and drug delivery. *Biomaterials* **28**, 4968-4977, doi:https://doi.org/10.1016/j.biomaterials.2007.08.006 (2007).
- 30 McKee, C. T., Last, J. A., Russell, P. & Murphy, C. J. Indentation Versus Tensile Measurements of Young's Modulus for Soft Biological Tissues. *Tissue Engineering Part B: Reviews* **17**, 155-164, doi:10.1089/ten.teb.2010.0520 (2011).
- 31 Lacour, S. P., Courtine, G. & Guck, J. Materials and technologies for soft implantable neuroprostheses. *Nature Reviews Materials* **1**, 16063, doi:10.1038/natrevmats.2016.63 (2016).
- 32 Chen, S. *et al.* Highly Flexible and Efficient All-Polymer Solar Cells with High-Viscosity Processing Polymer Additive toward Potential of Stretchable Devices. *Angewandte Chemie International Edition* **57**, 13277-13282, doi:doi:10.1002/anie.201807513 (2018).
- 33 Li, L. *et al.* A Solid-State Intrinsically Stretchable Polymer Solar Cell. *ACS Applied Materials & Interfaces* **9**, 40523-40532, doi:10.1021/acsami.7b12908 (2017).
- 34 Mok, J. W. *et al.* Network-Stabilized Bulk Heterojunction Organic Photovoltaics. *Chemistry of Materials* **30**, 8314-8321, doi:10.1021/acs.chemmater.8b03791 (2018).
- 35 Kim, T. *et al.* Flexible, highly efficient all-polymer solar cells. *Nature Communications* **6**, 8547, doi:10.1038/ncomms9547 (2015).
- 36 Yu, Y.-Y. *et al.* Intrinsically Stretchable Nanostructured Silver Electrodes for Realizing Efficient Strain Sensors and Stretchable Organic Photovoltaics. *ACS Applied Materials & Interfaces* **9**, 27853-27862, doi:10.1021/acsami.7b06963 (2017).
- 37 Wang, Z. *et al.* Intrinsically Stretchable Organic Solar Cells beyond 10% Power Conversion Efficiency Enabled by Transfer Printing Method. *Advanced Functional Materials*, 2103534, doi:10.1002/adfm.202103534 (2021).

- 38 Ks Narayanan, R. M. I. *Superior Multipurpose Adjuvant System for Rainfastness and UV Protection*. (ASTM International, 1996).
- 39 Knupfer, M. Exciton binding energies in organic semiconductors. *Applied Physics A* **77**, 623-626, doi:10.1007/s00339-003-2182-9 (2003).
- 40 Brédas, J.-L., Cornil, J. & Heeger, A. J. The exciton binding energy in luminescent conjugated polymers. **8**, 447-452, doi:10.1002/adma.19960080517 (1996).
- 41 Neamen, D. A. *Semiconductor Physics and Devices*. (McGraw-Hill, 2003).
- 42 Coropceanu, V. *et al.* Charge Transport in Organic Semiconductors. *Chemical Reviews* **107**, 926-952, doi:10.1021/cr050140x (2007).
- 43 Van Der Ziel, A. Noise in solid-state devices and lasers. *Proceedings of the IEEE* **58**, 1178-1206, doi:10.1109/proc.1970.7896 (1970).
- 44 Yang, D. & Ma, D. Development of Organic Semiconductor Photodetectors: From Mechanism to Applications. *Advanced Optical Materials* **7**, 1800522, doi:10.1002/adom.201800522 (2019).
- 45 Zhou, Y. *et al.* A Universal Method to Produce Low-Work Function Electrodes for Organic Electronics. *Science* **336**, 327-332, doi:10.1126/science.1218829 (2012).
- 46 Prince, M. B. Silicon Solar Energy Converters. *Journal of Applied Physics* **26**, 534-540, doi:10.1063/1.1722034 (1955).
- 47 Jr., W. J. P., Yoo, S. & Kippelen, B. Origin of the open-circuit voltage in multilayer heterojunction organic solar cells. *Applied Physics Letters* **93**, 193308, doi:10.1063/1.3027061 (2008).
- 48 Fang, Y., Armin, A., Meredith, P. & Huang, J. Accurate characterization of next-generation thin-film photodetectors. *Nature Photonics* **13**, 1-4, doi:10.1038/s41566-018-0288-z (2019).
- 49 Patterson, J. A. C., McIlwraith, D. C. & Yang, G.-Z. in *2009 Sixth International Workshop on Wearable and Implantable Body Sensor Networks* (IEEE, Berkeley, CA, USA).
- 50 Salvatierra, R. V., Cava, C. E., Roman, L. S. & Zarbin, A. J. G. ITO-Free and Flexible Organic Photovoltaic Device Based on High Transparent and Conductive Polyaniline/Carbon Nanotube Thin Films. **23**, 1490-1499, doi:10.1002/adfm.201201878 (2013).

- 51 Song, Y., Chang, S., Gradecak, S. & Kong, J. Visibly-Transparent Organic Solar Cells on Flexible Substrates with All-Graphene Electrodes. *Advanced Energy Materials* **6**, 1600847, doi:10.1002/aenm.201600847 (2016).
- 52 Chambon, S., Rivaton, A., Gardette, J.-L. & Firon, M. Photo- and thermo-oxidation of poly(p-phenylene-vinylene) and phenylene-vinylene oligomer. *Polymer Degradation and Stability* **96**, 1149-1158, doi:10.1016/j.polymdegradstab.2011.02.002 (2011).
- 53 Tournebize, A. *et al.* Impact of UV-Visible Light on the Morphological and Photochemical Behavior of a Low-Bandgap Poly(2,7-Carbazole) Derivative for Use in High-Performance Solar Cells. *Advanced Energy Materials* **3**, 478-487, doi:10.1002/aenm.201200662 (2013).
- 54 Fraga Domínguez, I., Topham, P. D., Bussi re, P.-O., B gu , D. & Rivaton, A. Unravelling the Photodegradation Mechanisms of a Low Bandgap Polymer by Combining Experimental and Modeling Approaches. *The Journal of Physical Chemistry C* **119**, 2166-2176, doi:10.1021/jp5103065 (2015).
- 55 St Onge, P. B. J., Ocheje, M. U., Selivanova, M. & Rondeau-Gagne, S. Recent Advances in Mechanically Robust and Stretchable Bulk Heterojunction Polymer Solar Cells. *Chem Rec* **19**, 1008-1027, doi:10.1002/tcr.201800163 (2019).
- 56 Cui, Y. *et al.* Over 16% efficiency organic photovoltaic cells enabled by a chlorinated acceptor with increased open-circuit voltages. *Nature Communications* **10**, doi:10.1038/s41467-019-10351-5 (2019).